THESIS FOR THE DEGREE OF DOCTOR OF PHILOSOPHY

High Temperature Corrosion of Stainless Steels in Low Oxygen Activity Environments

The effect of H_2 and H_2O

Hamed Hooshyar

Chalmers University of Technology

Department of Chemistry and Chemical Engineering
Chalmers University of Technology
Göteborg, Sweden 2016

High Temperature Corrosion of Stainless Steels in Low Oxygen Activity Environments

The effect of H_2 and H_2O

Hamed Hooshyar

ISBN 978-91-7597-329-6

© HAMED HOOSHYAR, 2016.

Doktorsavhandlingar vid Chalmers Tekniska Högskola
Ny serie nr 4010
ISSN: 0346-718X

Department of Chemistry and Chemical Engineering
Chalmers University of Technology
SE-412 96 Göteborg
Sweden 2016
Telephone +46 (0) 31- 772 2850
Hamed.hooshyar@chalmers.se

Cover:
BSE/SEM image of a NiCrAl exposed at 600 ^oC in 10% H_2- 20% H_2O- Ar.
''You can always see the science footprint in my research….if you have keen eyes!''

Chalmers Reproservice
Göteborg, Sweden 2016

High Temperature Corrosion of Stainless steels in Low Oxygen Activity Environments

The Effect of H_2 and H_2O

Hamed Hooshyar
Chalmers University of Technology

Abstract

Gasification of biomass and waste is promising for reducing the use of fossil fuels. While the operation conditions of superheaters and gas coolers in the gasifier are restricted by gas-side corrosion, scientific investigations are very scarce in this field. The corrosion of stainless steel (304L) and low-alloy steel (T22) in the 2 MW Chalmers gasifier was investigated. To understand corrosion in the real gasifier, simplified laboratory experiments were performed, focussing on the effect of H_2 and H_2O on different high temperature alloys. While 304L stainless steel showed protective behaviour in dry O_2 at 600˚C due to formation of a slow-growing $(Fe_xCr_{1-x})_2O_3$ oxide, it suffered rapid oxidation in $H_2 + H_2O + Ar$ environment at the same temperature. It is argued that "breakaway" oxidation was triggered by a deep chromium depletion of the alloy substrate. The chromium depletion was deeper in H_2-H_2O environment than it is in, e.g. dry O_2 because the pure chromia scale formed in H_2-H_2O environment grew faster that the $(Cr_{1-x}Fe_x)_2O_3$ scale formed in air and dry O_2. The ability of stainless steel to resist corrosion at high temperature relies on selective oxidation of chromium to form a slow-growing $(Fe_xCr_{1-x})_2O_3$ layer, the protective behaviour being the result of slow transport of ions through the oxide and the availability of chromium in the alloy. It is argued that if the alloy substrate becomes exhausted in chromium, another, faster mode of oxidation starts which is characterized by oxidation of iron to Fe^{2+}. The deep chromium depletion of the metal substrate is also accompanied by dissolution of oxygen into the metal and internal oxidation. The latter corresponds to a mixture of nm size FeCr spinel oxide particles and Fe,Ni metal. Compared to 304L, the highly alloyed stainless steel Sanicro28 and the FeCrAl alloy Kanthal APMT showed superior performance in $H_2 + H_2O + Ar$ environment. The corrosion resistance of Sanicro 28 is explained by its high Cr content which precluded a very deep Cr depletion of the alloy. The oxidation behaviour of Kanthal APMT was apparently almost the same in $H_2 + H_2O + Ar$ environment and in O_2.

Key words: High Temperature Corrosion, H_2O, H_2, pre-oxidation, chromia former, alumina former

Appended papers

The thesis is based on the following papers:

Paper I
H. Hooshyar, J. Liske, L-.G. Johansson, M. Seemann and T. Jonsson
"Initial Corrosion Attack of 304L and T22 in a 2MW Biomass Gasifier - A microstructural investigation"
Materials at High Temperatures, vol.32, issue 1-2, p: 198-204, 2015.

Paper II
H. Hooshyar, J. Liske, J-E. Svensson
"Process investigation of corrosion experiments at low oxygen activity environment containing H_2 /H_2O"
Proceeding at International Symposium of High-temperature Oxidation and Corrosion (ISHOC) 2014.

Paper III
H. Hooshyar, T. Jonsson, J. Hall, J. E. Svensson, L. G. Johansson, J. Liske
''The Effect of H_2 and H_2O on the oxidation of 304L- stainless steel at 600 ^oC: General behavior (part I)''
Oxidation of Metals, pp 1-22, online first, 2015, DOI 10.1007/s11085-015-9597-5

Paper IV
H. Hooshyar, M. Sattari, T. Jonsson, J. Liske, J-E. Svensson, L-G. Johansson
"A mechanistic study of high temperature oxidation of marginal chromia formers in presence of water vapor at low a(O_2) environment (Part II)"
Submitted to Oxidation of Metals

Paper V
T. Jonsson, S. Karlsson, H. Hooshyar, M. Sattari, J. Liske, J-E. Svensson and L-G. Johansson
"Oxidation after breakdown of the chromium rich scale on stainless steels at high temperature – internal oxidation''
Oxidation of Metals, pp 1-28, online first, 2016, DOI: 10.1007/s11085-016-9610-7

Paper VI
H. Hooshyar, T. Jonsson, J. Hall, J-E. Svensson, L-G. Johansson, J. Liske
"Oxidation behavior of several alloys in H_2-H_2O at 600 ^oC''
Manuscript

Paper VII
M. Sattari, H. Hooshyar, J. Liske, T. Jonsson
"The influence of a(O_2) on the base oxide of marginal chromia forming steels''
Manuscript

Statement of contribution

Paper I: I performed all of the experimental and analytical work except the gas analysis which was performed by Martin Seemann. I authored the paper with support from my supervisors.

Paper II: I performed all of the experimental and analytical work. I authored the paper with support from my supervisors.

Paper III: I performed all of the experimental and analytical work except the AES analysis which was performed by Dr. Josefine Hall. I authored the paper with support from my supervisors.

Paper IV: I performed all of the experimental and analytical work except the TEM analysis which was performed by Dr. Mohammad Sattari. I authored the paper with support from my supervisors.

Paper V: I performed the exposures on 304L in the H_2-H_2O environment, XRD analysis, SEM/EDX analysis and assisted in the interpretation of the results.

Paper VI: I performed all of the experimental and analytical work except the AES analysis which was performed by Dr. Josefine Hall. I authored the paper with support from my supervisors.

Paper VII: I performed all of the experimental work and assisted in interpretation of results and writing the paper.

Related Work

Related papers not included in this thesis:

- E. Sadeghimeresht, H. Hooshyar, N. Markocsan, P. Nylén
  ‘’Oxidation performance of NiCoCrAlY HVAF-sprayed coating in H_2-H_2O environment’’
  Manuscript

- E. Sadeghimeresht, H. Hooshyar, N. Markocsan, P. Nylén
  ‘’Ni and NiCr HVAF-sprayed coatings; Characterization and oxidation behavior in H_2-H_2O environment’’
  Manuscript

Preface

This thesis summarizes the research carried out within the Swedish Competence Centre for High Temperature Corrosion (HTC), from 2011-2016. The work was performed at the Division of Energy and Materials at the Department of Chemistry and Chemical Engineering, Chalmers University of Technology, Gothenburg, Sweden, under the supervision of Professor Lars-Gunnar Johansson. The work was funded by the High Temperature Corrosion Centre (HTC) and by Chalmers Area of Advance Energy and the Swedish Energy Agency (SEA).

List of acronyms

AES	Auger Electron Spectroscopy
BCC	Body-centred cubic
BIB	Broad Ion Beam
BSE	Backscattered Electron
EDX	Energy Dispersive X-ray spectroscopy
EELS	Electron Energy Loss Spectroscopy
FCC	Face-centred cubic
FIB	Focused Ion Beam
HAADF	High Angle Annular Dark Field
OM	Optical microscopy
SE	Secondary Electron
SEM	Scanning Electron Microscopy
STEM	Scanning Transmission Electron Microscopy
TEM	Transmission Electron Microscopy
XRD	X-Ray Diffraction

Table of Contents

1. Introduction

Concerns about global warming and increasing CO_2 emissions have motivated increased use of green energy, e.g., wind power, solar power and the use of renewables instead of fossil fuels. In Sweden, the transformation to a sustainable society started as early as the 1990's, and, today, the use of fossil fuels for heat and power production is minor. However, in the transportation sector (i.e. fuels for vehicles), fossil fuels still dominate. In order to increase the share of green fuels in the transportation sector, the utilization of biogas from the thermal gasification of biomass and waste is a key issue.

In general, the term *gasification* refers to a chemical process in which any carbonaceous fuel is converted to a gaseous fuel [1]. Compared to combustion, the available oxygen in the environment is deficient [2] for the complete conversion of hydrocarbons, and the resulting gaseous products are dominated by species like H_2 (g) and CO (g). A variety of other gas species increase the complexity of the environment enormously thus it includes water vapour, alkali chlorides, sulphides, as well as possible fly ash or aerosols. The chemical composition of the produced gas dictates the boundaries within which, e.g., superheaters and product gas coolers will operate. Due to the presence of the mentioned species, corrosion problems in the gasification of the biomass/waste-to-energy industry is often severe. This is because of the difficulty in developing protective oxides, such as Cr- and Al-rich corundum-type oxides, on the steel components applied in these high temperature environments [3]. Corrosion studies in biomass/waste gasification is scarce, therefore, it is of great importance to increase our knowledge about the complex corrosion processes occurring in the steels used in these environments.

Currently, low alloy steels and stainless steels are widely used in power plants. The ability of especially stainless steels to form a thin protective Cr-rich corundum-type oxide, make them a good choice for use in high temperature applications. The oxide acts as a barrier layer, separates the alloy and the environments, and results in a significant decrease in the material corrosion rate. The other alternative for use in high temperature corrosive environments is alumina formers. As in the case of chromia formers, these steels can form a thin protective Al_2O_3 which is also able to suppress further corrosion of the material. However, as mentioned above, in aggressive environments, the development of these protective oxides may be hindered, and, thus, this may result in crucial degradation of the material.

In order to approach these complex corrosion issues, this thesis includes a general investigation of the initial corrosion behaviour of two types of steels (304L and T22) in a 2MW Chalmers gasifier (one set of exposure), as a first step, and a more detailed investigation of the corrosion behaviour of broader range of steels by means of well-controlled laboratory exposures. The field exposures were aimed at providing relevance (both with respect to environmental parameters and the extent of the corrosion) whereas the laboratory exposures were aimed at providing knowledge about the corrosion attack/mechanism.

In order to better understand the complex corrosion reactions that occurred in the field exposures, laboratory exposures were performed in more simplified and well-controlled environments. Since H_2 and H_2O can be found in many energy systems, such as combustion engines, the anode side of solid oxide fuel cells and steam power plants as well as gasifiers, the laboratory exposures mainly focused on environments containing H_2 and H_2O. In the literature, several mechanisms have been proposed to address the effect of these two gases in low $p(O_2)$ environments. However, this is not fully understood yet. Thus, the effect of H_2 and H_2O was investigated in microscopic detail for 304L-stainless steels as a major part of this study with the aim of understanding the mechanism behind the oxidation of marginal chromia formers in H_2-H_2O containing environments. One way to mitigate a corrosion attack is to use more corrosion resistant material. Thus, in addition to the detailed study mentioned above, the general corrosion behaviour of Sanicro 28, two grades of 304L and Kanthal® APMT were also briefly investigated.

2. Materials

2.1. Steels

Steel is a generic name for iron alloys containing carbon in the range of 0.005 wt% to 2 wt%. The carbon content of steels is kept low whenever properties like high ductility, toughness, and weldability are favoured, but is kept high when high strength, hardness, fatigue, and wear resistance are required [4]. Alloy steels are steels to which alloying elements (like chromium, nickel, manganese etc.) have been added to improve steel properties [5]. Alloyed steels can be commonly divided in to three groups; low-alloy steels, high-alloy steels (stainless steels), and tool steels.

Iron is the major component of the steels which can have two crystal structures below its melting point. From room temperature to 912 ºC, ferrite (α) is the thermodynamically favoured form of pure iron. The crystal structure of ferrite is body-centred cubic (bcc), see Fig. 1. Iron has a bcc crystal structure from 1394 ºC to 1530 ºC, which is known as δ-ferrite. At 912 ℃, the crystal structure of pure iron transforms to face-centred cubic and forms austenite (γ) [4]. It should be noted that the transformation temperature is not the same for the alloys and is dependent on the content of carbon and alloying elements. During transformation from ferrite to austenite, the carbide present in the material is dissolved. During cooling, the size and distribution of particles can be controlled, which leads to greater material strength. Martensite is the third possible crystal structure that can be obtained in steels in which the atoms are arranged in a body-centred tetragonal form. Martensite is not thermodynamically stable at room temperature, but since the carbon diffusion is insignificant at this temperature, transformation to the ferrite phase is slow.

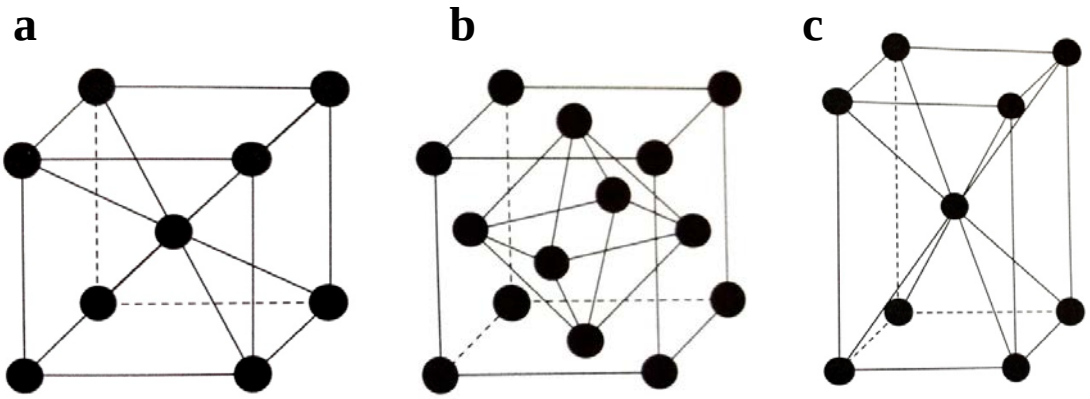

Fig. 1. a) Ferrite (body-centred cubic), b) Austenite (face-centred cubic) and c) Martensite (body-centred tetragonal).

Chromium is the major element added to steels to improve corrosion properties. Stainless steels contain at least 11 weight percent of chromium [6]. The corrosion resistance of stainless steels comes from the formation of a chromium-rich oxide layer which acts as a protective barrier and decreases further oxidation of the material. Stainless steel can be in ferritic, austenitic and martensitic form. The 304L stainless steel used in this thesis (both laboratory and field exposures) was austenitic. Nickel is added to the alloy and acts as an austenite stabilizer.

Syngas coolers is one of the most crucial and highly loaded components in gasification plants. This is due to the high pressure and temperature in addition to the presence of corrosive gases. These parameters impose challenging requirements for material selection. Composite tubes are one example of materials used for syngas coolers. The outer part of those tubes which is faced toward the corrosive gases is mostly made up of austenitic stainless steel, and the inner part is ferritic, which has greater strength than austenitic steel. Thus the inner part provides good strength resistivity toward the high pressure inside the tube and of course induced stress corrosion cracking.

304L austenitic stainless steel, which is often used as a reference material for corrosion exposures, was investigated in both the laboratory and field exposures. It contains approximately 18 weight percent of chromium, see Table 1. As can be seen in the table, two different grades of 304L were used in the laboratory studies. The major difference between these two grades is their chemical compositions.

Sanicro 28 is a high alloy austenitic stainless steel with a Cr and Ni content of 27 and 31 wt%, respectively, see Table 1. Sanicro28 was used in the laboratory studies to obtain a general understanding about the oxidation of the alloy in H_2-H_2O at 600 ºC.

T22 ferritic steel, which is considered as a low alloy steel, was only investigated in the field exposures. It contains about 2 weight % of chromium. Table 1 shows the chemical composition of the steels used in this study.

2.2. Alumina forming alloys

FeCrAl

FeCrAl alloys are used preliminary in high temperature applications (900-1300 ºC), such as industrial furnace furniture. These alloys are used in shielding tubes and uncooled components in coal-, gas-, and biofuel-fired power plants. FeCrAl alloys are ferritic, and their crystal structure is in the form of body-centered cubic (bcc), see Fig. 1. The ability of these alloys to form a highly protective alumina layer at a quite low level of aluminium content has made these alloys interesting for usage in corrosive environments. The chromium and aluminium contents of these alloys are in the range of 19-22 and 1-5 wt%, respectively. The chromium is added to the alloy to decrease the critical aluminium content needed to form a protective alumina layer at elevated temperatures and also to improve the ductility of the alloy [7-9].

In the present study, Kanthal APMT (see Table 1), which is a commercial alloy, was used in the laboratory studies in H_2-H_2O at 600 ºC.

Table 1. Chemical composition of the investigated materials. The concentrations are in wt. %.

Composition [wt%]	Cr	Al	Mo	C	Mn	Si	Minor Add.	Fe	Ni
APMT	22	5	3	≤0.05	≤0.4	≤0.7	Present	Bal.	-
304L(18/8)	18.18	-	0.53	0.022	1.53	0.31	Present	Bal.	8.10
304L(18/10)	18.5	-	0.49	0.027	1.41	0.55	Present	Bal.	10.2
Sanicro 28	27	-	3.5	0.02	2	0.7	Cu	Bal.	31
T22	2.19	-	0.93	0.095	0.49	0.26	Present	Bal.	-

3 Oxidation Theory

From the corrosion aspect, oxidation is one of the most important reactions occurring at high temperatures. The oxidation of a metal can occur in both high and low oxygen activity environments and can be described as a reaction occurring between oxygen and metal to form a metal oxide. But different parameters can affect the oxidation behaviour, and, in most cases, the oxidation mechanism is complicated and not easy to interpret. The oxidation starts with an oxide nucleation and continues with the growth of an oxide scale. The most important parameter for the formation of an oxide is its thermodynamic stability, which will be discussed in the next chapter.

3.1 Oxide Formation

In most environments, metals are not thermodynamically stable and are prone to form oxides, nitrides, carbides, etc., depending on the environment. In a dry oxygen atmosphere, oxide formation at room temperature is very slow. However, the oxidation rate increases with increasing temperature. Therefore, the corrosion resistivity of metals is important at elevated temperatures. The oxide formation of metals can be written as:

$$aM(s) + (b/2)O_2\,(g) \longleftrightarrow M_aO_b \qquad (1)$$

It appears that the oxidation reaction can be regarded as one of the simplest chemical reactions, but, in most cases, the oxidation behaviour and mechanism are not easy to investigate in detail. Oxide formation can be divided into different steps:

- Adsorption of gas on the metal surface (see Fig. 2A).
- The formation of a separate oxide nuclei and consequently a thin oxide layer in addition to the dissolution of the gas in the metal (see Fig. 2B)
- Growth of film/scale (see Fig. 2C)

The first and the second steps are dependent on different parameters such as: surface orientation, crystal defects on the metal surface, surface preparation, and the existence of both metal and gas impurities.

When a thin film layer forms on the metal surface, the driving force may be due to the charge gradient, and the limiting factor will be surface reactions. The driving force changes to a chemical potential gradient when a thick layer is formed, and the solid-state diffusion of

reactants will become the limiting factor. These three steps of oxide formation are illustrated in Fig. 2:

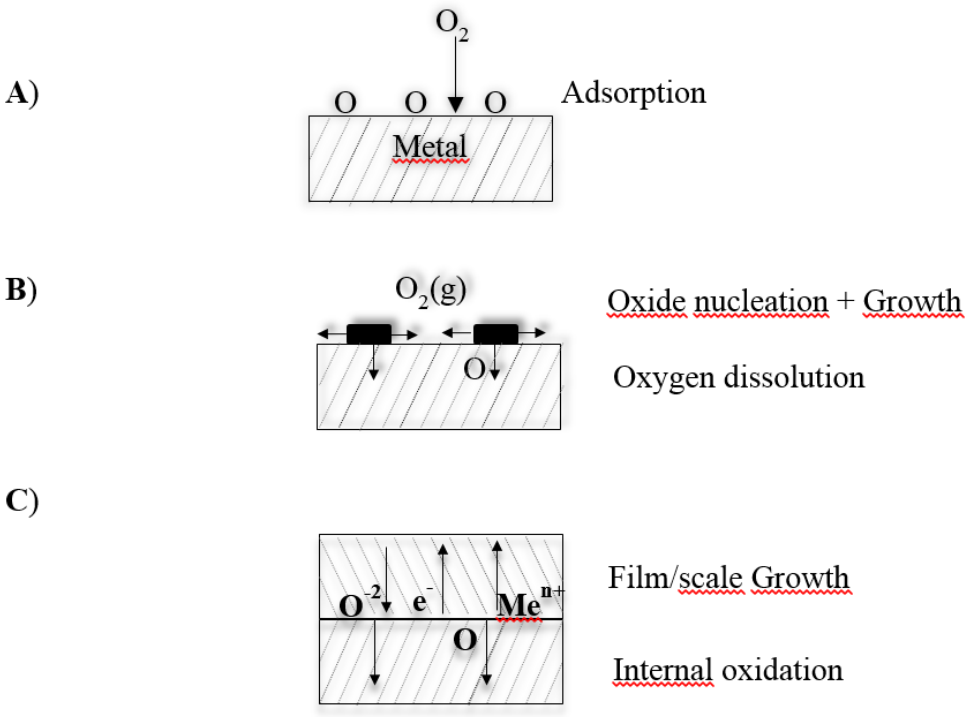

Fig. 2. Schematic illustration of oxide formation [10].

3.2 Thermodynamics

The oxidation reaction between oxygen gas and a metal can be written as Reaction 1. Based on thermodynamics, an oxide will form on a metal surface when the oxygen partial pressure of the environment is higher than the oxygen partial pressure in equilibrium with the oxide. The latter is also referred to as the dissociation pressure of the oxide. This is defined by the standard free energy of oxide formation:

$$\Delta G^\circ = -RT\ln(a_{MO2} / a_M\, p(O_2)) \qquad (2)$$

Where a_{MO2} and a_M are the oxide and metal activity, respectively, and $p(O_2)$ is the partial pressure of the oxygen gas. In general, the activity of different elements in the alloy is defined by the equation below:

$$a_M = \gamma_M * X_M \qquad (3)$$

where γ_M and X_M are the activity coefficient and molar fraction of the metal M in the alloy, respectively. In the ideal condition, γ_M is equal to one. Pure liquids and solids have the activity of unity at one bar, thus Equation (2) can be written as follows:

$$\Delta G^\circ = -RT\ln p(O_2) \quad (4)$$

Fig. 3 shows the Elingham diagram. The oxygen partial pressure needed for metals to form an oxide at a certain temperature can be extracted from the Elingham diagram [11].

In low oxygen activity environments, like environments consisting of H_2 and H_2O, the H_2/H_2O ratio can be used to identify the oxygen pressure needed for the formation of the metal oxide (see Equation 6). For example, if the H_2/H_2O ratio is equal to 0.5, the oxygen activity of the environment at 600 °C will be about 5×10^{-24}. Thus at that temperature, the oxides with a lower dissociation pressure than 5×10^{-24} will be thermodynamically stable.

As can be seen in Equations 5 and 6, the equilibrium oxygen partial pressure of an environment containing hydrogen and water vapour is defined by the H_2/H_2O ratio.

$$2H_2O \longleftrightarrow 2H_2 + O_2 \quad (5)$$

$$p(O_2) = \left\{\exp\left(\frac{-\Delta G^\circ}{RT}\right)\right\}\left(\frac{pH_2}{pH_2O}\right) \quad (6)$$

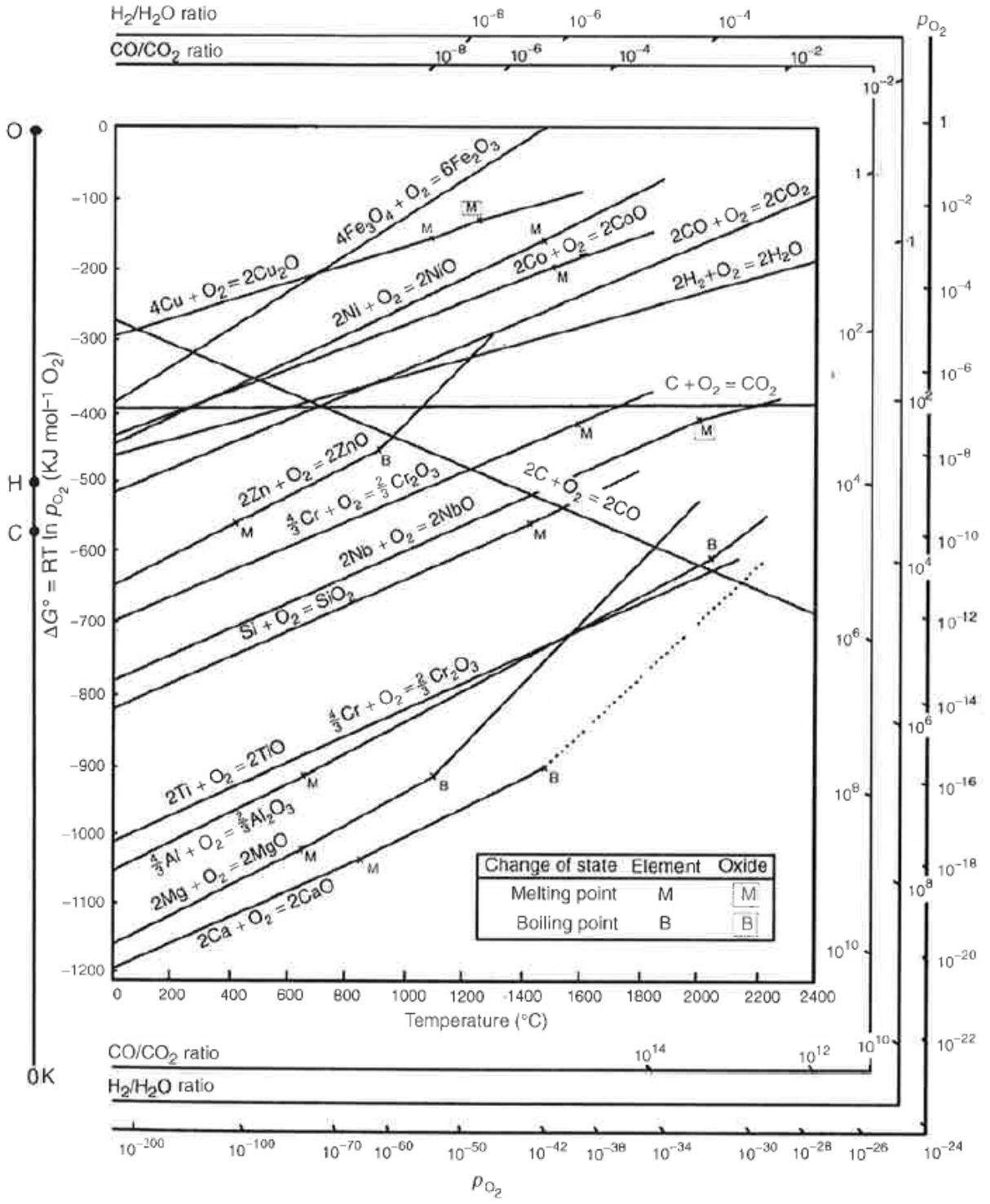

Fig. 3. Ellingham diagram, variation of free energy vs temperature for different oxides [12].

3.3 Defects

Solid reaction products formed during high temperature oxidation may have different microstructures and morphologies. The microstructure and morphology of an oxide depends on

various parameters, such as the chemical composition of the metal and oxidant, temperature, and reaction conditions. The reaction product can be in the form of dense and continuous films/scales. In more severe cases, the compact scale may fail to develop or it may initially form and then rupture and beak up.

When dense films/scales are formed, the metal and the oxidant are separated. Thus, the oxidation process may only proceed by the solid state diffusion of the reactants through the films/scales. The overall oxidation reaction will then take place either by means of the solid state transport of the reactants atoms or ions, or by the transport of electrons (if the oxide is ionic conductor). Diffusion of electrical charges occurs due to the presence of defects in an oxide. Thus it is necessary to know about the defects in oxidation products in order to understand the oxidation mechanism at high temperatures and also how water vapour/hydrogen may affect this mechanism [10].

Solids contain different compositional and structural defects which are mainly categorised in three main groups: Point defects, line defects (dislocations), and plane defects, such as grain boundaries, phase boundaries, and external surfaces.

A point defect is an imperfection which is limited to one structural or lattice site. It can be in the form of vacancies in the crystal structure due to a missing atom or in the form of interstitial atoms sitting between the regular sites. When the concentration of point defects in the lattice is high, they may associate or cluster and, consequently, form a larger defect. Line defects (or dislocations) are the imperfections caused by the misplacement of atoms in certain directions in a lattice. Planar defects comprise internal interfaces, such as grain boundaries, phase boundaries, stacking faults, and external interfaces, such as surfaces [10].

In addition to the structural defects described above, crystals can also contain electronic defects, i.e., electrons and holes which can freely move in the crystal.

As a general rule, metal oxides show deviations from exact stoichiometry. If a nonstoichiometric oxide is oxygen deficient and the single point defects are the main defects in the oxide, these will form oxygen vacancies. On the other hand, if the oxide contains excess metal, interstitial metal ions will be formed. In both cases, the defects, if charged, will contain positive charges and will need the equivalent negative defects (electrons) for compensation. Such nonstoichiometric oxides are termed as n-type semiconductors. In contrast, nonstoichiometric oxide can be deficient in metal or have an oxygen excess. These defects, if

charged, will contain negative charges and need the equivalent positive defects (electron holes) for compensation. These oxides are called p-type oxides [10].

3.4 Diffusion

As mentioned in the previous section, as the oxidation process proceeds, a dense scale forms and separates the material bulk from the environment. Thus the continuation of the oxidation will be a result of the solid state diffusion of the reactants and electrons through the scale. Diffusion can occur through the lattice, grain boundaries, or other diffusion paths. Also during oxide growth, additional phenomena may happen. Based on the oxidation mechanism, this can result in the formation of cavities, porosities, micro cracks, etc., in the bulk and/or oxide. These features can also affect the transport of the reactants through the oxide [10]. The growth of oxide by means of lattice diffusion has been described well by Wagner [13], which will be discussed in the next chapter. Lattice diffusion is assumed to occur due to the presence of point defects such as vacancies, interstitial ions, electrons, and electron holes, see Fig. 4 [10]. Different kinds of lattice diffusion are shown in Fig. 5.

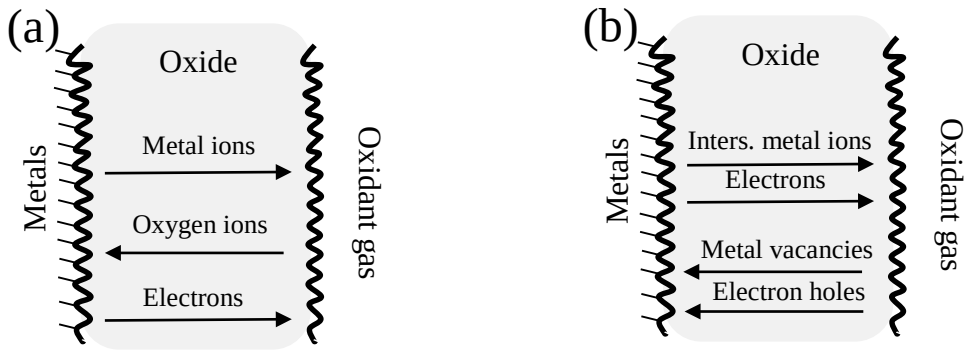

Fig. 4. (a) Transport process through a dense, single-phase scale growing by means of lattice diffusion. (b) Transport processes in growing scales by means of lattice and electronic defects [10].

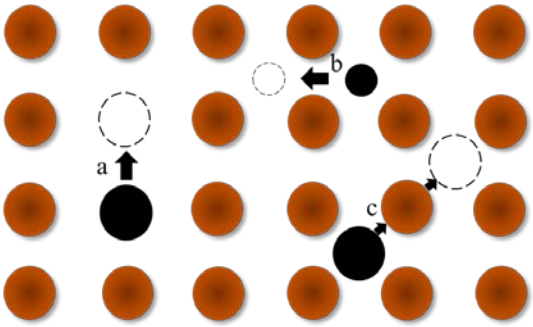

Fig. 5. Different types of lattice diffusion; a) vacancy diffusion, b) interstitial diffusion, c) interstitialcy diffusion [11]**.**

In addition to lattice diffusion, diffusion can also occur along a line or surface defects such as dislocations, grain boundaries, inner and outer surfaces, etc. These transport paths are termed high diffusivity paths since they are faster than lattice diffusion. Also, since grain boundary and dislocation diffusion have lower activation energy than lattice diffusion, they are more important at lower temperatures [7, 10].

3.5 Kinetics

The Ellingham diagram and other thermodynamic calculations determine the possibility of a certain oxide formation at a specific temperature, but they do not give us information about the rate of the reaction. In some cases, the formation of an oxide is thermodynamically possible but its rate is low. Therefore, knowing about the kinetics of an oxidation reaction is necessary when it comes to understanding the corrosion behaviour of a metrial. In addition, if there is a possibility of different oxide formations occurring, e.g., in an alloy, the thermodynamics calculation alone cannot predict which oxide will be formed on the material. Thus, a combination of thermodynamics and kinetics information can help us to obtain a better understanding of an oxidation behaviour and mechanism [11]. Oxide growth may be defined in terms of linear, logarithmic, and parabolic rate laws, see Fig. 6.

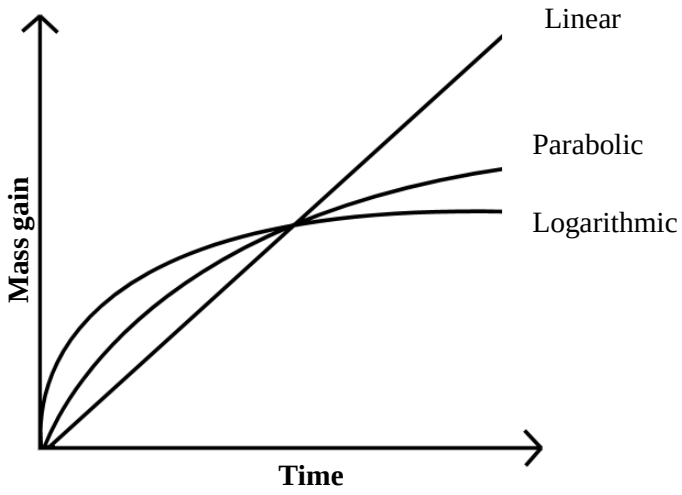

Fig. 6. Mass gain curve versus exposure time for three common oxidation mechanisms.

Logarithmic Growth: This law usually includes the oxidation of thin layers. Most metals exposed at low temperatures, generally below 300-400 ^{o}C, exhibit logarithmic behaviour. The speed of the reaction is fast initially but becomes slow after some time [11], see Fig. 6. The rate determining step is generally believed to be the transport of electrons or ions from the metal through the oxide to the adsorbed oxygen atoms at the sample surface [10].

$X=K \log t + A$ Direct Logarithmic (8)

$1/X = B K' \log t$ Inverse Logarithmic (9)

(X= oxide thickness, t = time, K= direct logarithmic constant, K´ = inverse logarithmic constant)

Parabolic Growth: Many metals and alloys exhibit parabolic behaviour at high temperatures. This mechanism can be explained by continuous decrease in the oxidation rate as the oxide grows, see Fig. 6. Thus the oxidation rate has an inverse relation with the thickness of the oxide [11].

$dX/dt=K_p /X$ (10)

Or

$X^2= 2 K_p t + C$ (11)

(X = oxide thickness, t = time, C= integration constant, K_p = parabolic rate constant)

The parabolic growth mechanism has been explained by Wagner [14] assuming that:

- The oxide is compact and adherent.
- Ion diffusion through the oxide scale is the rate-controlling process of the mechanism.
- There is a local equilibrium at the metal/oxide interface and the gas/oxide interface.
- Oxygen solubility in the metal is negligible.

Linear Growth: For some metals, the oxidation rate is constant with time. In such a mechanism, the reaction speed is in direct relation with time [11], see Fig. 6.

$$dX/dt = K_t \quad (12)$$

or

$$X = K_t t + D \quad (13)$$

(X= oxide thickness, t = time, K_t = linear rate constant, D = constant)

In a strongly oxidizing condition, a thick, dense, and adherent layer is formed, which leads the growth to a parabolic behaviour. But in a low oxidizing environment, like in CO/CO_2 mixtures, a linear growth mechanism has been observed. As the oxide layer grows, porosity and micro-cracking develop, which reduces the protectiveness of the film. Thus the parabolic growth law may fail after a short time, and the kinetics of the reaction will change to the linear law. Either the surface reaction or phase boundary reaction controls the reaction rate in this oxidation model. Also diffusion through a protective layer of constant thickness can lead to a linear reaction rate.

4 Corrosion Products

Although the oxidation of alloys is more complex than that of pure metals, some of the factors described for the oxidation of pure metals can also be applied to alloys. Some of these complexities can be due to: different affinities of metals for oxygen, the formation of ternary or higher oxides, different mobility of metal ions in the oxide, different diffusivity of metals through the alloy, etc. [15].

At high temperatures, alloys commonly form different oxides within a scale. The properties of the oxides, consequently, define the general corrosion properties of the alloys. For instance, if a dense, continuous and protective oxide layer forms, it will largely decrease the rate of further oxidation of the material. The properties of some of the most important corrosion products of the alloys used in this study are summarized below. The formation of the different oxide layers in an alloy is correlated to several parameters, such as temperature, the chemical composition of the alloy, the environment in which the material is exposed etc. As an example, in low oxygen activity environments, like in the H_2-H_2O environment used in this study, some oxides (e.g. hematite) which have a higher oxide dissociation pressure than the environment, are thermodynamically unstable and, therefore, do not form on the alloy.

Fe_2O_3, Hematite

Fe_2O_3 has two different crystal structures: α- Fe_2O_3 and γ- Fe_2O_3. Hematite (α- Fe_2O_3), which has a corundum-type structure, is significant above 400 °C. In corundum type structures, oxygen anions form hexagonal closed packed lattices in which the metal cations fill two thirds of the octahedral holes. In the temperature range 650-800 °C, the oxide acts as an n-type semiconductor, and it behaves as a p-type semiconductor at higher temperature ranges. Hematite is the most stable phase at low to medium temperatures and in high oxygen activity environments, but it is not thermodynamically stable in environments with low oxygen activity. Hematite is expected to behave as a protective oxide compared to other iron oxides, but its protectiveness is not comparable with Cr_2O_3.

Fe_3O_4, Magnetite

Magnetite is less protective than hematite, but it is more stable at lower oxygen activity environments . It contains both divalent (Fe^{2+}) and trivalent (Fe^{3+}) iron. At room temperature,

magnetite has an inverse spinel-type structure in which the oxygen anions occupiy the face-centred cubic arrays. One eighth of the tetrahedral holes in an oxygen sub lattice is occupied by half of the trivalent ions (8 Fe^{3+}). The octahedral holes in the oxygen sub lattice are filled with the rest of the ions (8 Fe^{3+} and 8 Fe^{2+}). Magnetite acts as an n-type semiconductor. At low oxygen activities, the oxide contains cation excess and metal interstitials are the significant defects [10].

Cr_2O_3, Eskolaite

Eskolaite is the most stable form of chromium oxide at high temperatures. It has a corundum-type structure and behaves as a p-type semiconductor. Unlike hematite, it is thermodynamically stable in lower oxygen activity environments. In a polycrystalline material, it has been shown that chromium diffusion is dominated by grain boundaries especially at temperatures below 1000 ^oC. In high oxygen activity environments and at relatively high temperatures, eskolaite behaves as a protective layer in, e.g., stainless steels. However, it has been shown that any process which leads to a chromium depletion in the Cr_2O_3 layer, can significantly decrease the protectiveness of the layer.

$(Fe, Cr)_2O_3$, Corundum type solid solution

Hematite and eskolaite are iso-structural and can be solved in each other and form an oxide solid solution $(Fe_xCr_{1-x})_2O_3$. The protectiveness of the oxide layer depends on the chromium content of the layer, and, as mentioned above, any process which causes chromium depletion in the protective layer, will increase the corrosion rate in high oxygen activity environments. Asteman[16] has shown that an oxide behaves like : a p-type semiconductor where x= 0- 0.25, an n-type semiconductor where x= 1 and both an n-type and a p-type where x= 0.25- 0.75.

$(Fe,Cr,Ni)_3O_4$, Spinel-type solid solution

In stainless steels which contain Cr and Ni together with Fe, a mixed spinel-type solid solution can form. The solid solution can have both an inverse and a normal spinel structure. Since the size of the Fe, Cr, and Ni ions are roughly the same, they can dissolve in many combinations. However, this also depends on the alloy composition and the oxygen activity of the environment.

Al_2O_3, aluminium oxides

Alumina exists in various forms at different temperatures. However, it is only α-Al_2O_3, with a corundum structure, which is the thermodynamically stable form of aluminium oxide. The other forms of alumina (γ, δ and θ) are termed transient alumina and are comparatively less protective than α-Al_2O_3. The transient oxides are formed at lower temperatures and may transform to α-Al_2O_3 with time, temperature, and alloy composition. For instance, when Cr is added to the alloy, it acts as a nuclei and accelerates the transformation from a transient θ-Al_2O_3 to a stable α-Al_2O_3 [17, 18]. The general understanding about α-Al_2O_3 is that it forms at about 1000 ºC [10, 19, 20], however, it has been reported [21, 22] that it can form at 700 ºC on FeCrAl alloys in dry O_2 after 168 hours.

Alumina (Al_2O_3) is thermodynamically more stable than chromia (Cr_2O_3). Also, continuous alumina scales grow slower than Cr_2O_3. Therefore, the former shows better corrosion resistanance when alumina scales are selectively oxidised from aluminium constituents. However, if the selective oxidation of aluminium does not occur, aluminium is oxidised internally and forms, for instance, beneath the Cr_2O_3 layer [10].

5 Corrosion in the presence of H_2 and H_2O

It has been shown in the previous studies that the oxidation rate of pure iron, pure chromium and chromia forming alloys is higher in the presence of water vapour. Below is a brief summary of the effect of water.

Oxidation of pure chromium in the presence of H_2O and/or H_2

Quaddakers et al. [23] have found that the oxidation rate of pure chromium in H_2-H_2O-Ar is faster than in air. The oxide exhibited fewer tendencies to buckle and more tendencies to form whiskers on top of the scale than in air.

Hänsel et al. [24] have shown that when pure chromium is exposed to H_2-H_2O-Ar at 1000 ºC, chromia blades grow on the scale surface. The same behaviour was not seen when it was exposed to O_2-H_2O at the same temperature. It was also found that at low $p(O_2)$, increasing the $p(H_2O)$ increases the oxidation rate when $p(H_2)$ is kept constant. At a fixed $p(H_2O)/p(H_2)$ ratio, the oxidation rate is enhanced by increasing the $p(H_2O)$ level. The authors have shown that the oxidation rate does not change significantly by increasing the water vapour in a high oxygen partial pressure environment. However, it changes considerably with $p(H_2O)$ when chromium is exposed to H_2-H_2O. This is explained by the local surface catalysis of water vapour dissociation in a low $p(O_2)$ environment, where molecular oxygen is minor. If the transport of chromium is rapid, it causes a local acceleration in the rate of chromium oxidation in addition to the formation of chromia blades.

Other studies [25-27] have shown a more rapid oxidation rate for pure chromium in the presence of H_2O than in dry O_2. Henry et al. [25] have suggested that this is due to the faster diffusion of hydroxide ions (ionic radius of OH^-: 95pm) compared to oxygen ions (ionic radius of O^{2-}: 140 pm). Hultquist et al. [26] have suggested that it can be because of the easier dissociation of H_2O than O_2 and also a hydrogen uptake by chromium, which leads to a higher cation (metal) diffusion. The authors have shown that when chromium contains dissolved hydrogen prior to the exposure, the oxidation rate increases when exposed to both O_2 and H_2O [28]. Pujilaksono et al. [27] have claimed that even in the Hänsel results an increase in the oxidation rate of chromium can be seen at high $p(O_2)$. Pujilaksono et al. have pointed out that since blade formation was found in his own results even in an environment with high $p(O_2)$, it could not be because of the reduction of water on the surface. Instead he has suggested that a transition occurs from a poorly crystalline to a well-texture crystalline structure in the chromium oxide at

a critical oxide thickness, and that hydroxylation of the oxide on the surface due to the presence of water are the main reasons for the blade formation. The author has suggested that hydroxylated chromium is more mobile than surface chromium ions coordinated to oxide ions, which is due to the weakening of some Cr-O-Cr bonds as a result of hydroxylation. The faster surface diffusion of Cr ions subsequently affects the growth of oxide grains.

Oxidation of pure iron in the presence of H_2O and/or H_2

Young et al [29] have reported that when pure iron is exposed to H_2-H_2O at the temperatures 800-1200 ºC, the oxidation rate increases by increasing $p(O_2)$ at fixed $p(H_2O)$. However, the oxidation rate of iron is almost independent of $p(H_2O)$. The mass transport has been suggested to be due to the contribution of both cation vacancies and hydroxyl species.

Rahmel and Tobolski [30] have shown that increasing water vapour at high $p(O_2)$ environments, increases the oxidation rate of pure iron at 950 ºC. However, the authors have found that the oxidation rate is independent of $p(H_2O)$ at 750 ºC. The systematic study of the effect of water vapour on pure iron at lower temperatures is scarce; however, there are a few studies that investigate this issue. Pujilaksono et al. [31] have reported that at high $p(O_2)$, the addition of water vapour increases the oxidation rate of pure iron at 500 and 600 ºC while it somewhat reduces the rate of oxidation at 400 ºC. It was also found that the morphology of hematite is strongly affected by the presence water vapour. In their study, the tendency for the formation of a needle- and blade-shaped oxide on top of the scale was greater in the presence water vapour at 400 and 500 ºC. The same morphology dependency was not seen at 600 ºC. Because of the similarities between the hematite and chromia, the authors have suggested that the same phenomena may explain the blade formation on pure chromium [27] can be used for pure iron as well. Thus, the hydroxylation of iron oxide on the surface increases the mobility of iron ions, and the preferential growth of the minimum energy surfaces of hematite leads to the blade formation.

Wallinder et al. [32] have also reported that the oxidation rate of pure iron exposed to O_2 at 500 ºC and 700 ºC is enhanced when hydrogen is present in the metal prior to exposure.

Oxidation of Fe-Cr alloys and steels in the presence of H_2O and/or H_2

Several studies have been performed to address the effect of water vapour and oxygen partial pressure on Fe-Cr alloys in high and low $p(O_2)$ environments [27, 33-41]. However, studies of these two parameters in a low $p(O_2)$ environment at temperatures below 700 ºC are scarce. It has been reported that the oxidation rate of the alloys increase by increasing the $p(H_2O)$ at a fixed $p(H_2)$, and also with $p(O_2)$ at a constant $p(H_2O)$. When a sufficient amount of chromium is present in the alloy, the chromium-rich oxide that forms on the surface of the alloy can protect the material even in the presence of corrosive species, such as water vapour. However, if the chromium content lies below the critical level for the formation of the protective layer, the corrosion accelerates and usually leads to breakaway oxidation. Several mechanisms have been suggested to explain the effect of water vapour on Fe-Cr alloys; however, the mechanisms are still under debate. Below is a summary of these mechanisms is provided. Since some of the mechanisms that have been discussed in the literature are somewhat similar, only a few examples will be discussed further for each mechanism.

I) Dissociative mechanism

Fuji et al. [42, 43] have investigated the oxidation of Fe-Cr alloys (1 to 15 wt% Cr) exposed to Ar- 10% H_2O at 700 ºC -1100 ºC. The oxide scale was characterised by an outer wustite layer, an inner porous spinel-wustite layer, and a subscale spinel layer. It was found that the wustite layer detached extensively from the inner spinel-wustite layer, and, also, the alloy suffered from a high rate of oxidation. Therefore, it was suggested that the dissociative process was responsible for the oxidation mechanism and that hydrogen seems to play a significant role in the internal voids as an oxygen carrier. The schematic of the mechanism is shown in Fig. 7. At Interface I, H_2O dissociates and the oxygen produced at the surface react with the iron ions produced from the dissociation of FeO at Interface II. Most of the hydrogen was desorbed but some of them was dissolved in the oxide. The permeated hydrogen reacted with the oxygen at Interface II and produced H_2O in the void between I and II. H_2O acted as an oxygen carrier gas and reached Interface III. Therefore, the same process that happened at Interface I will also occur at Interface III. The process, which occurs at the metal/oxide interface, is complicated; however, it is driven by the production of metal ions and defect removal in the oxide. The rate determining step in this mechanism is the surface reaction and not the diffusional transport,

although the transport of Fe ions from the metal to the oxide/gas interface is limited to the oxide bridges present between the two oxide layers.

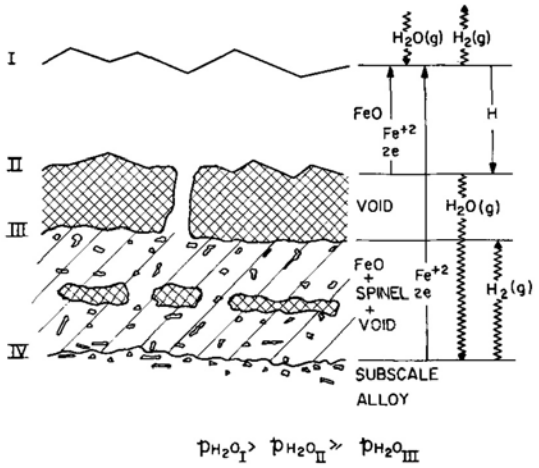

Fig. 7. Fuji's proposed dissociation mechanism for Fe-Cr alloys in water vapour at high temperature [42]**.**

Rahmel and Tobolski [30] have proposed a somewhat similar mechanism. The main difference between the dissociation mechanism and the H_2/H_2O bridge formation proposed by Rahmel and Toboloski is that the rate determining step of oxidation is the reaction at the oxide/gas interface and gas/crack interface in the former and latter cases, respectively [44].

II) Faster oxygen diffusion via OH^- rather than O^{2-}

Henry et al. [41] have investigated the oxidation of ferritic steels exposed to Ar-15% O_2 and Ar- 15% H_2O at 900 ºC. The authors [25, 41] have suggested that, due to the lower radius of OH^- (95 pm) compared to that of O^{2-} (140 pm), the transport of the former species is faster than latter ones. This idea has also been proposed by Nickel et al. [45]. Consequently, the effect of $p(H_2O)$ can be associated with an increase in the concentration of hydroxide species in the oxide. In addition, it has been suggested that breakaway oxidation occurs due to the depletion of chromium at the alloy/scale interface. As an oxygen species reaches the chromium depleted region, the nucleation and growth of Fe-rich oxides occur.

There are three proposed mechanisms for this failure [46, 47]:

- Vaporization-induced failure
- Chemical failure

- Mechanically-induced chemical failure

Henry et al. [41] have reported that vaporisation can not be the reason for failure since chromium evaporation is negligible in this exposure condition (Ar- 15% H_2O). Although the chemical concentration of chromium at the metal/oxide interface in Henry's results is higher than the calculated critical chromium content, the author nevertheless suggests that the chromium depletion at the metal/oxide interface can play a role in this failure. The author also suggested that the effect of water vapour is coupled with a mechanical effect.

III) Chromium evaporation

Asteman et al. [47] have shown that when 304L stainless steels are exposed to O_2+ 10% H_2O at 600 ºC up to 672 hrs, a mass loss occurs. This was not the case when the same samples were exposed to dry O_2. The mass loss has been explained by the evaporation of chromium species from the surface, probably in the form of $CrO_2(OH)_2$. The chromium evaporation was confirmed by the author by means of analysing the species condensed on a cooled probe installed at the end of the exposure furnace.

The same author [39, 48] has also reported that increasing the flow rate at a fixed water vapour content, has the same effect as a higher concentration of water vapour. Their results showed that most of the sample surface was covered with a protective $(Fe,Cr)_2O_3$ layer at low flow rates (at 700 ºC) even in the presence of water vapour. However, as the flow rate was enhanced, the protective behaviour was lost, and the whole surface was covered by a thick iron-rich scale. It has been claimed that the flow rate dependency can strengthen the chromium evaporation mechanism for the breakaway oxidation of chromia formers and marginal chromia formers in the presence of water vapour.

IV) Proton defects in the oxide lattice

Hultquist et al. have shown that the oxidation rate of pure chromium in O_2 [26, 49] and H_2O [26] and also pure Fe in O_2 [32] at high temperatures increases when hydrogen is present in the sample prior to the exposure. This has been explained by an increase in cation diffusion due to the formation of a more defective oxide when hydrogen is present in the metal. Since Fe and Cr oxides are the main oxides formed on stainless steels, it has been claimed that hydrogen can have the same effect on stainless steels too. The authors [32] have also mentioned that another

possible effect of hydrogen, in the case of pure iron, could be a decrease in Fe-Fe bond strength which would lead to a more rapid diffusion of metal

Nakagawa et al. [50] have shown that when ferritic steels were oxidised in a steam/air dual atmosphere, the oxidation rate on the air side increases considerably compared to a single air atmosphere. It has been suggested that this increase is due to the permeation of hydrogen from the steam side. As the hydrogen reaches the voids at the metal/oxide interface on the air side, the dissociation mechanism (discussed above) causes the acceleration in the oxidation process.

Nakai et al. [51] reported that the oxidation rate of Fe-10Cr-0.08C at 600 ºC was enhanced in presence of water vapour. But the oxide thickness for pure Fe exposed to dry and wet O_2 at the same temperature is comparable. Since the amount of measured dissolved hydrogen in a ferritic steel is higher than pure iron, it has been claimed that hydrogen dissolution in the oxide may change the defect structure of the oxide and, consequently, cause an increase in ionic diffusion. Thus this would explain the acceleration in the oxidation of ferritic steels in the presence of water vapour.

V) Microcracks in initially formed Cr_2O_3

Schutze et al. [52, 53] have found that water vapour has a significant influence on the oxidation of 9% Cr steels (investigated in dry air and air up to 10% H_2O). The authors suggest that this can have two main reasons: First, chromium evaporation, and, second, the scale growth stresses (even in isothermal exposures), which lead to scale micro-cracking and subsequent crack healing. Both cases lead to chromium depletion on a metal surface beneath the initial oxide due to the formation of chromia by simple oxidation. Schutze's measurements reveal that the scale stresses increase significantly in the presence of water vapour. This can explain the increase in cracking and the rehealing of the oxide caused by the presence of H_2O. Therefore, it has been suggested that the accelerated oxidation in H_2O can be caused by the interaction between the oxidant and chromium depleted zone in the metal.

VI) Volatile Fe-hydroxides

Ehlers et al. [34] have investigated the oxidation behaviour of 9% Cr steel P91 exposed to N_2-O_2-H_2O at 650 ºC. It was found that the transition from the initial protective oxide to a non-protective oxide is related to the H_2O/O_2 ratio rather than the absolute value of H_2O (g). It was

suggested that scale growth is governed by the competitive absorption of H_2O and O_2 on the internal and external oxide surfaces and also by the formation of volatile Fe-hydroxide that takes place during transient oxidation. To describe the effect of volatile Fe-hydroxide, it was assumed that H_2O permeates the scale and a gas/oxide equilibrium is achieved. Since $p(O_2)$ is lower at the inner layers, more Fe-hydroxide is produced and the gradient of $p(Fe(OH)_2)$ at the inner and outer surfaces leads to the outward diffusion of $Fe(OH)_2$. $Fe(OH)_2$ is not stable at higher $p(O_2)$ and, consequently, it deposits as solid oxides in the form of hematite or magnetite, see Fig. 8.

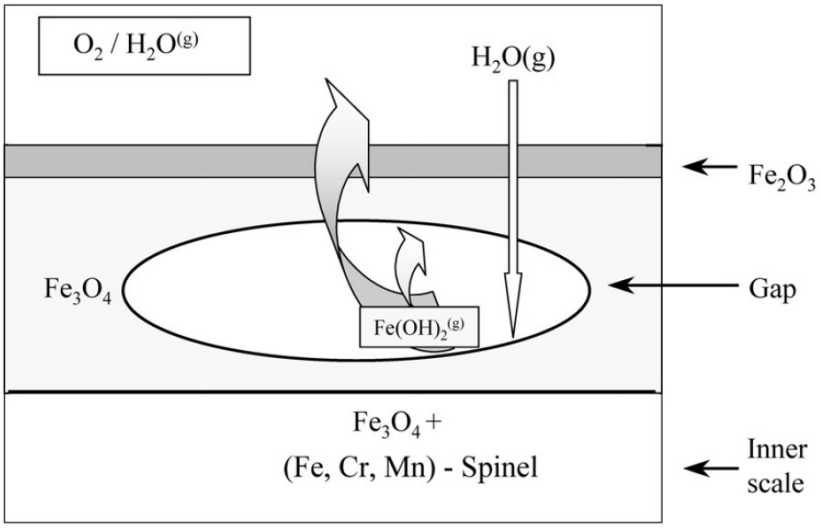

Fig. 8. Schematic illustration of volatile Fe-hydroxide proposed by Ehlers et al.[34].

The value of $pFe(OH)_2$ at 650 ºC is about 10^{-11} atm [54] of oxygen potentials in the magnetite stability range. This value is too low to provide a considerable mass transport; however, since this value was extrapolated from higher temperatures, Ehlers suggests that a more reliable thermodynamic calculation is needed to confirm it. The author suggestes that due to the presence of void and also the thickening of the oxide above the void, a solid oxide diffusion of species is impossible. Instead, it has been proposed that hydroxide species provides an outward vapor-phase transport of iron.

VII) Tendency of Cr to oxidise internally

Essuman et al. [55] have investigated binary Fe-Cr alloys at 900 ºC in Ar-O_2, Ar-H_2O, Ar-H_2-H_2O. They suggest that chromium is more prone to oxidise internally in the presence of water vapour. Thus, the formation of the outward protective Cr-rich oxide is suppressed and

breakaway oxidation occurs. The authors claim that in addition to the effect of water vapour on Cr-evaporation, the void formation and changing transport processes in the oxide scale, water vapour can also affect the transport processes in the alloy. Since hydrogen from water vapour can permeate ferritic steels at high temperatures [50], it has been assumed that hydrogen has an influence on one (or more) of the essential parameters which promote(s) the formation of an external chromia layer. The findings were [56], that hydrogen is more likely to affect $N_O^{(s)}$ (oxygen solubility) and/or D_O (oxygen diffusivity) rather than $D_{Fe\text{-}Cr}$ (alloy interdiffusion coefficient) or K_p (parabolic rate constant). The proposed mechanisms for these two affected parameters are: First, the inward diffusion of hydrogen in to the alloy shifts the $O\text{-}H_2\text{-}H_2O$ equilibrium on the alloy surface towards a higher oxygen concentration and, consequently, leads to a higher inward flux of oxygen into the alloy. Second, the inward diffusion of hydrogen expands the iron lattice and, therefore, increases the oxygen diffusivity in the alloy. Thus, the tendency of Cr to oxidise internally in the presence of water is an ‘’easy’’ explanation for the oxidation of alloys with an intermediate Cr content.

Effect of water vapour on (Fe/Ni)CrAl alloys

Studies of the influence of water vapour on the oxidation behaviour of (Fe/Ni)CrAl at 600 ºC are scarce. However, it is known that, as in the case of chromia formers, a higher amount of aluminium is needed for the selective oxidation of Al_2O_3 on an alumina former in the presence of water vapour than in dry atmospheres [10]. Israelsson et al. [57] have shown that when a FeCrAl alloy Kanthal® APMT is exposed at 600 ºC and 700 ºC, the oxidation rate is somewhat faster in the presence of water vapour than in dry oxygen. In both cases, a thin oxide was formed which was dominated by alumina in addition to a significant amount of iron and chromium. No crystalline aluminas could be detected in the scale using the XRD technique, which was in agreement with previous studies [21, 58] conducted on FeCrAl alloys at 500 and 600 ºC. A higher rate of oxidation of Kanthal® AF [59] was also observed in the presence of water vapour at 900 ºC. The scale formed in both dry and wet atmospheres contained sub-layer α-alumina. The top layer, in both cases, consisted of γ-alumina which was converted to $\gamma\text{-}Al_{2-x}(Mg,Fe)_{xO3-(x/2)}$, $MgAl_2O_4$, and $\alpha\text{-}Al_2O_3$ after some time in dry oxygen. It has been suggested [59] that stabilisation of γ-alumina layer by hydroxylation of γ-alumina in present of water vapour is the main reason for such an acceleration.

6 Corrosion in gasifier plants

The oxygen content in combustion environments is sufficiently high in order to form, e.g., different iron and chromium oxides. As mentioned in the previous chapters, if a protective oxide is thermodynamically stable to form, further attack from the gaseous environment is mitigated when the layer is developed on the alloy surface. However, in a reducing environment (such as a gasifier environment), the formation of such a protective layer may be hindered, and, other corrosive components, like sulphur and chlorine, will better opportunities to corrode the metals [60]. In addition, gas species, such as H_2, H_2O, CO, CO_2, CH_4, some other hydrocarbons, H_2S and HCl are also available in the syngas cooler environment. The presence of these gases can cause other types of corrosion, like carburization [61], sulphidation and chlorination[60].

There are several studies available that investigate corrosion problems in the gasification of coal, but corrosion studies on biomass and waste gasification are scarce. The main differences between coal and biomass as fuels are: the higher chlorine and water content and lower sulphur and ash content in biomass than in coal. However, oxygen and carbon activity are supposed to be similar [62].

Källström et al. [60] have performed a field exposure in a Studsvik 2MW gasifier in which municipal/ industrial waste was used as fuel. Those authors have reported that iron- and nickel-based alloys show similar corrosion rates and chlorine and sulphur act as corrosion accelerators. However, no sign of carburization was seen in their samples.

Bakker et al. [63] have investigated the corrosion of syngas coolers in coal gasification. According to that study, sulphidation is the major corrosion process for low alloy steels and is rather independent of the presence of chlorine. For high alloy steels with a chromium content of about 20%, the authors mention two different types of corrosion; Type A and Type B. In Type A corrosion, which occurred in the HCl-free environment, the corrosion increased as a function of $p(S_2)/p(O_2)$. At higher ratios of $p(S_2)/p(O_2)$, a rather protective $FeCr_2S_4$ layer was found to form on alloys 800 (20Cr-32Ni-Fe) and 310 (25Cr-20Ni-Fe). At lower ratios, $FeCr_2O_4$ formed instead. In the presence of HCl, Type B corrosion occurred on alloy 800. The corrosion was found to be independent of the $p(S_2)/p(O_2)$ ratio and a FeS outward growing oxide formed on top of an inward growing Cr_2O_3 layer containing Fe(Ni)S. The oxide scales showed a non-protective behaviour. The authors conclude that the corrosion related to high temperature sulfidation alone is sufficiently low for alloys containing about 20% Cr to provide acceptable

long-term service. However, in the presence of high chlorine-rich deposit, the authors suggest that spallation may occur which could lead to accelerated corrosion.

7 Experimental and analytical techniques

7.1 Sample preparation

The chemical composition of the stainless steel, 304L, is provided in Table 1. Metal coupons with an area of 5.56 cm^2 (15 × 15 × 2 mm coupons with a 1.5 mm hole in the top middle of the samples) were cut and ground with SiC papers to 1000 mesh. Afterwards, they were polished with diamond paste down to 1 µm. The samples were degreased and cleaned with water, acetone, and ethanol using ultrasonic agitation. The sample preparation was performed with a Struers machine. Prior to the exposure time, the samples were stored in a desiccator.

7.2 Exposures

7.2.1 Furnace exposure

Exposures were performed in tubular furnaces (see Fig. 9) with the gas flow set to 200 ml/min (equal to 0.8 cm/min). The furnace was equipped with an alumina tube, and samples were placed in an alumina sample holder standing parallel to the flow. A peristaltic pump was calibrated precisely and used as the water supplier. It is important to note that, in high oxygen activity environments when oxygen is available in percentages, oxygen leakage from any part of the system does not have an outstanding effect on the corrosion mechanism but this leakage becomes important when the oxygen activity of the system is set to low values. Therefore for this study, different exposure processes were tested (using oxygen and a humidity sensor) to achieve the optimum process to get rid of impurity traces available in the environment and thus provide the intended low oxygen activity. Three samples were put in the furnace in each exposure series and different H_2 and H_2O contents were run at different times.

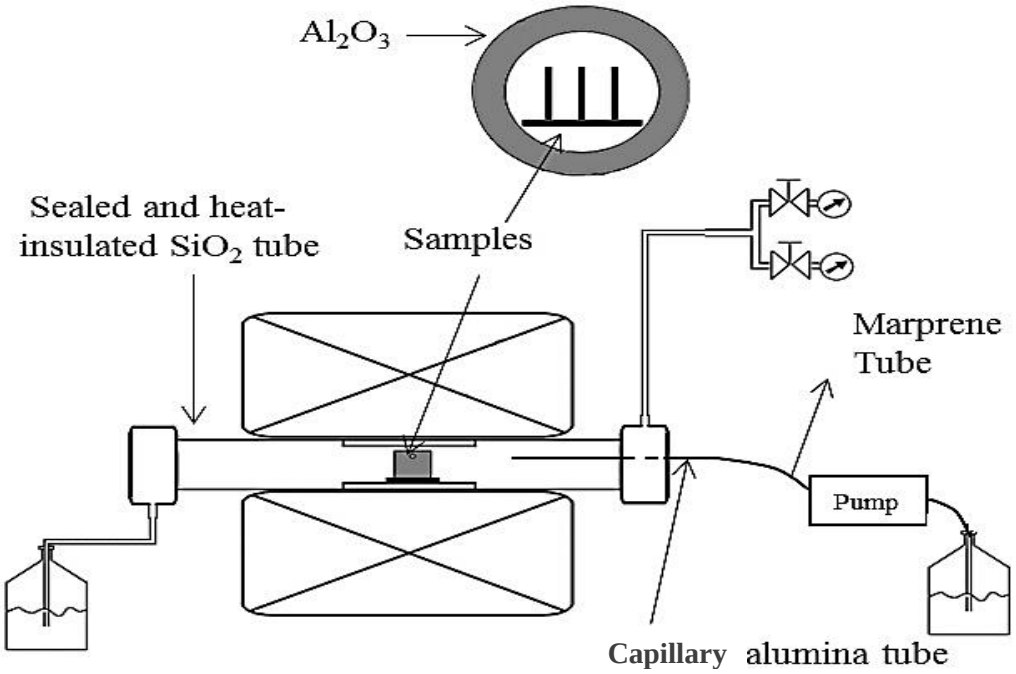

Fig. 9. Schematic image of the horizontal furnace system.

7.2.2 Field Exposure

Exposures performed in a 2MW Chalmers gasifier, see Fig. 10. In the present study, wood chips were used as fuel. The probe used in the field exposure was connected to a control unit in which the temperature for each sample was set. The probe was also connected to a nitrogen supplier to cool the probe tip and the samples to the intended temperature. The probe could take up to four sample coupons with an area of 1 cm^2 (10*10*2 mm) in each exposure. Fig. 10 shows the schematic of the Chalmers boiler and gasifier. The place in which the exposure was performed is marked with a red box. The schematic of the probe can be seen in Fig. 11.

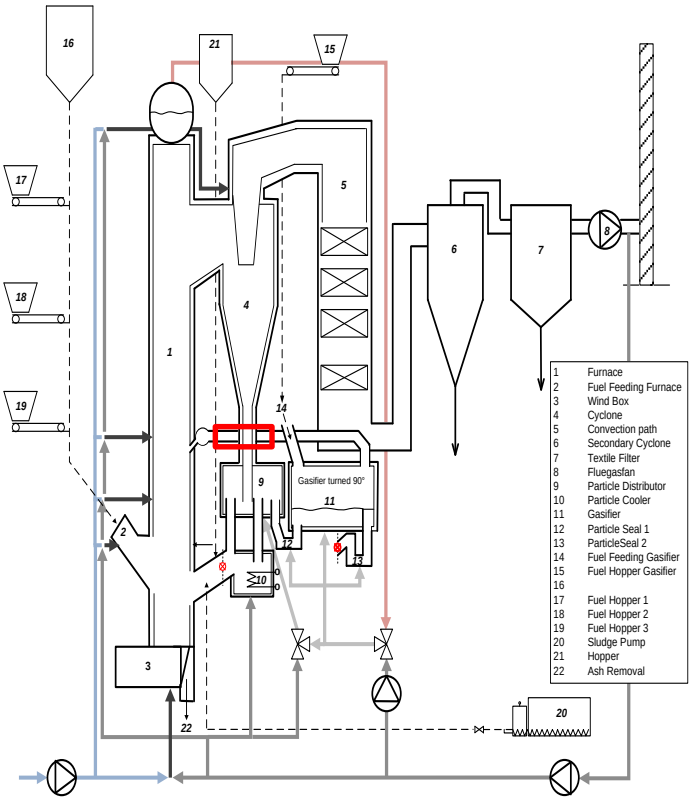

Fig. 10. Schematic image of Chalmers boiler and gasifier, Gothenburg.

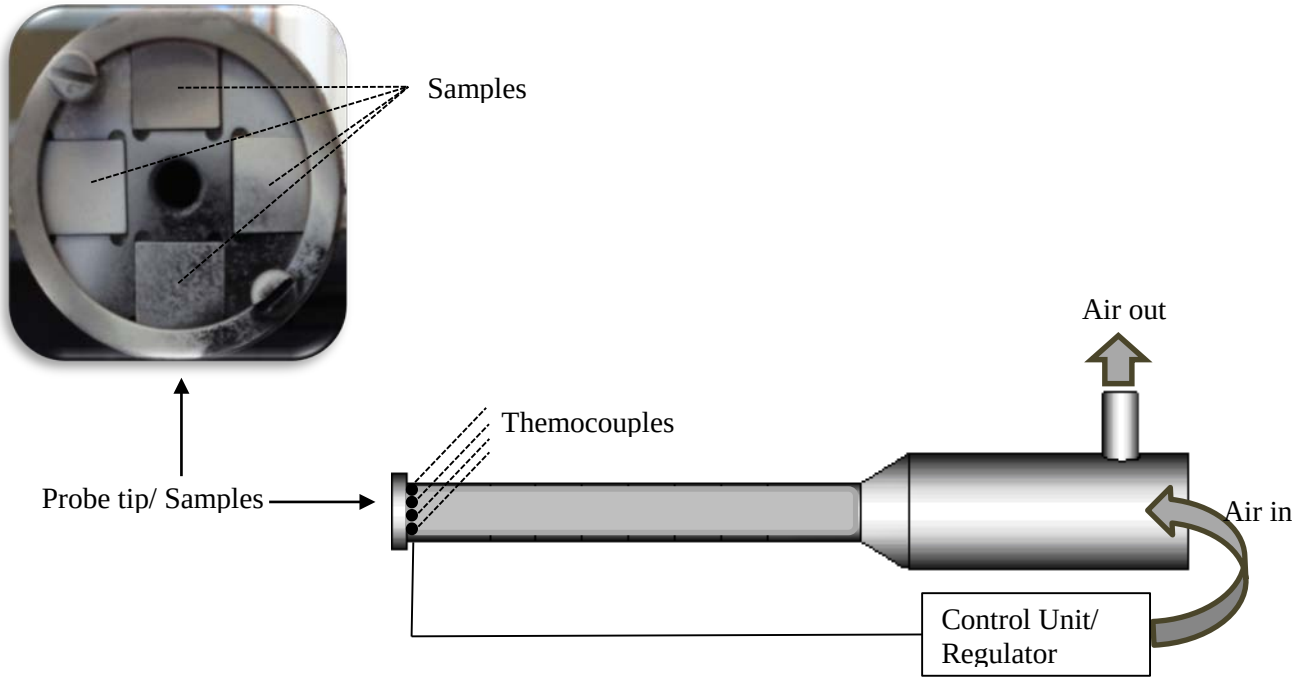

Fig. 11. Schematic image of corrosion probe used in field exposure.

8 Analytical techniques

Applying different analytical techniques is essential for a better understanding of oxidation/corrosion behaviour. Each technique has its own advantages and disadvantages, thus, in most cases, it is crucial to combine different techniques to come to a scientific conclusion. Different analytical techniques used in this research will be described in this chapter.

8.1 X-Ray Diffraction (XRD)

This technique can be used to identify different crystalline phases present in an oxide scale. The theory underlying the technique is that, first, the sample is bombarded with a focused beam of monochromatic X-rays. Then a constructive interference of the X-ray occurs when the diffracted photons satisfy Bragg's Law, i.e., when the path length difference between two waves is equal to an integer (n) of the X-ray wavelength (λ) (see Equation 14).

$$n\lambda = 2d_{hkl}\sin\theta \qquad (14)$$

n: order of reflection (integer number)
λ: wavelength of X-rays
d_{hkl}: interplanar spacing of lattice planes
$\theta = (\theta_1 + \theta_2)/2$

The wavelength is known and the angle of incident θ is measured using the XRD machine. Thus by comparing the d values with the tabulated ones, crystalline phases of a sample can be detected [15]. In this study, a Siemens D5000 powder diffractometer (equipped with grazing incidence and a Göbel mirror) was employed to detect different crystalline oxide phases.

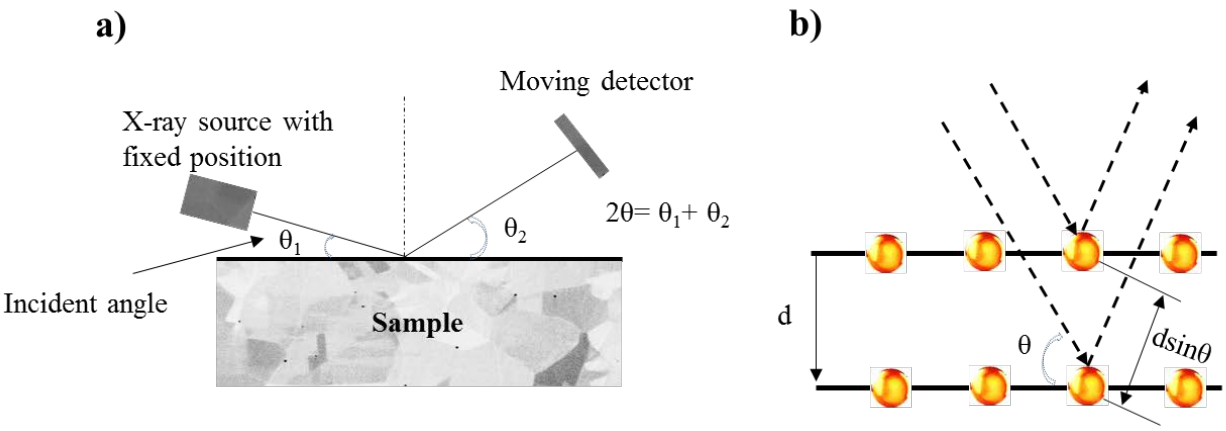

Fig. 12. a) Setup of grazing incidence X-ray diffraction. b) Diffraction illustration by crystal planes which fulfil Brag's Law.

In the present study, Cu Kα (λ= 1.5418 Å) was used, and the angle of incidence was in the range of 1 to10° based on the thickness of the oxide scale, with 20< 2θ< 70.

8.2 Scanning Electron Microscope (SEM)

A scanning electron microscope allows for the investigation and characterization of different materials on micro and nano scales. High resolution and large depth of focus are two main advantageous of SEM which permit the user to conduct a detailed study of the sample. In an SEM, a finely focused electron beam scans the intended area to form images. Secondary electrons, backscattered electrons, characteristic x-rays, and other protons of various energies are different types of signals produced by the interaction of the electron beam with a sample (see Fig. 13). Two important signals that can be obtained using SEM are secondary and backscattered electrons. Secondary electrons provide information about the topography, while backscattered electrons provide information about chemical composition and density of the sample. Characteristic x-rays can be achieved as a result of electron bombardments and give both qualitative identification and quantitative elemental information with a resolution of about 1µm in depth and 1µm in diameter in normal operating conditions [64]. In this research, a FEI Quanta 200 ESEM FEG was widely used equipped with an Oxford Inca EDX system. The accelerating voltage used was in the range of 10 to 20 kV for imaging and mostly 12 kV was used for EDX analysis. A Zeiss Ultra 55 FEG SEM was also used for higher resolution imaging of thin oxides.

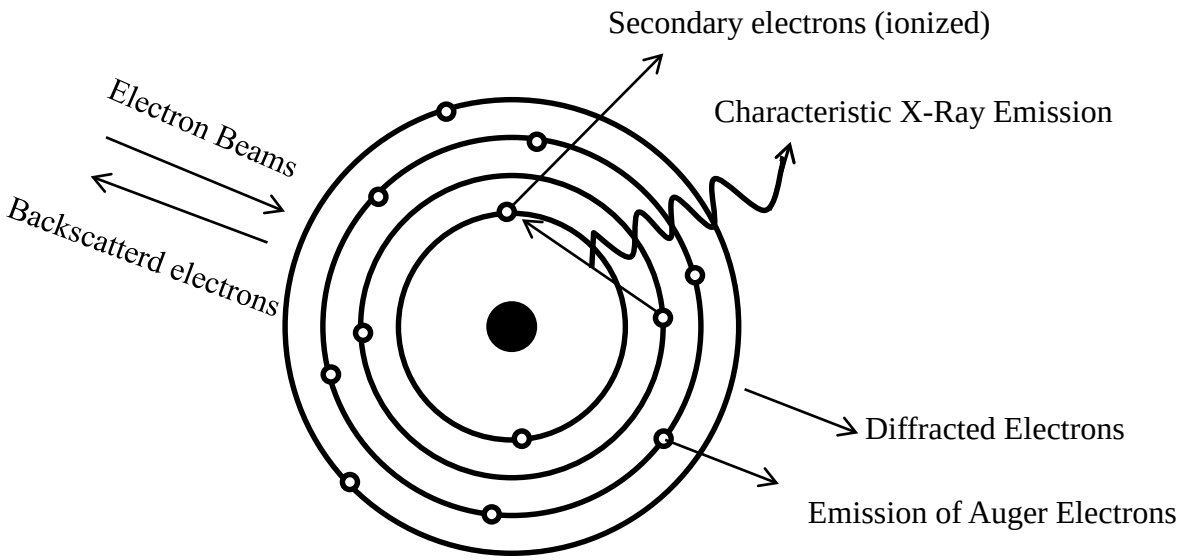

Fig. 13. Electron beam interaction with atoms [65].

8.2.1 The design of the SEM

Fig. 14 illustrates the schematic of a standard SEM. Electrons are generated and accelerated by an electron source. Before reaching the sample, electrons pass through different lenses and apertures which focus the electron beam. The aim is to make the probe size as small as possible while maintaining a high current of electrons [66].

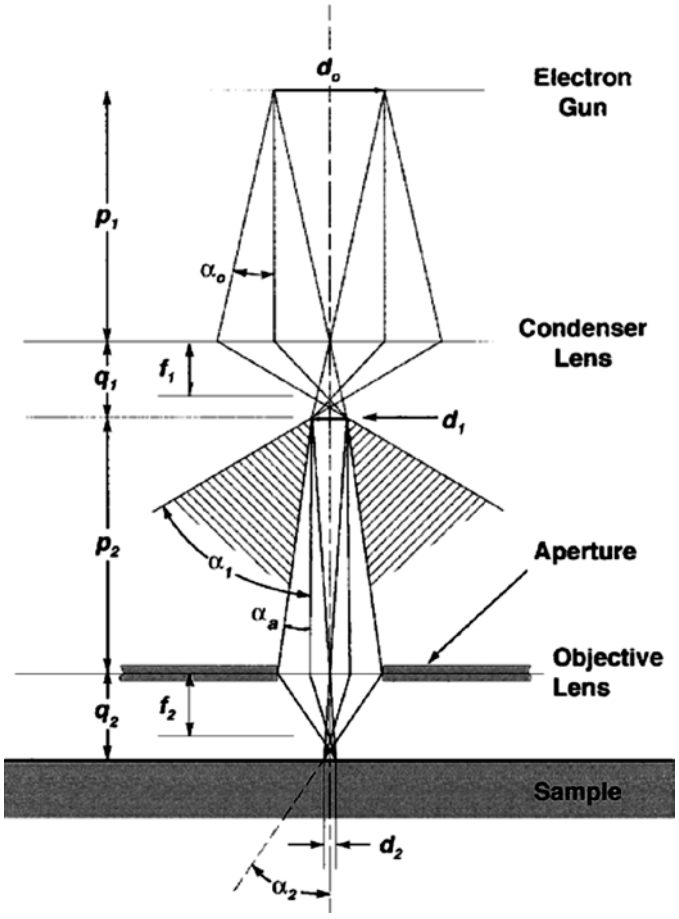

Fig. 14. Schematic of SEM column with aperture, condenser and objective lenses [64].

8.2.2 Secondary Electrons (SE)

Secondary electrons (SE) have low energy (<50eV) and can be emitted from the regions close to the sample surface (<10 nm). Thus a high resolution image can be achieved in which the contrast represents the sample topography. The contrast is caused by the ‘’edge effect’’, since more electrons are emitted from edges of a sample than from the flat surfaces and show up as brighter features [66].

8.2.3 Backscattered Electrons (BSE)

Backscattered electrons have higher energy (>50 eV) than secondary electrons, therefore these electrons can be generated from a larger volume (0.1-0.5 μm). However, their spatial resolution is lower. The contrast obtained in BSE images is related to the chemical composition, density and geometry of the sample. Elements with a higher atomic number emit more BSEs and will appear brighter [66].

8.3 Energy Dispersive X-Ray (EDX)

If an electron beam has enough energy to emit an electron from the inner electron shell of an atom, another electron from the outer shell will be replaced and the atom will relax by emitting a photon (see Fig. 13). Since each electron shell of a specific atom has a specific energy, the generated x-ray will have a characteristic energy which is the energy difference between the two shells and this can be used to identify the chemical composition of a sample. X-rays can be generated from even larger volumes than BSEs. Figure 11 presents the interaction volume from which different signals are generated. It should be noted that lightweight elements are difficult to quantify with EDX with high accuracy, since they emit low energy x-rays. Even for heavy elements some corrections should be made to achieve accurate quantification. ‘’ZAF’’ correction is one of the corrections which should be considered in which ‘’Z’’ represents the atomic number which affects the scattering, ‘’A’’ represents absorption (photons can be absorbed by a sample), and ‘’F’’ represents fluorescence (exciting other types of atoms) [66]. Although it is possible to decrease the accelerating voltage to obtain a better spatial resolution for x-rays, the energy of an electron beam needs to be sufficiently high to emit electrons from the inner shell of an atom [64]. It is also possible to perform map and line analysis with EDX which show the elemental distribution of, e.g., an oxide scale.

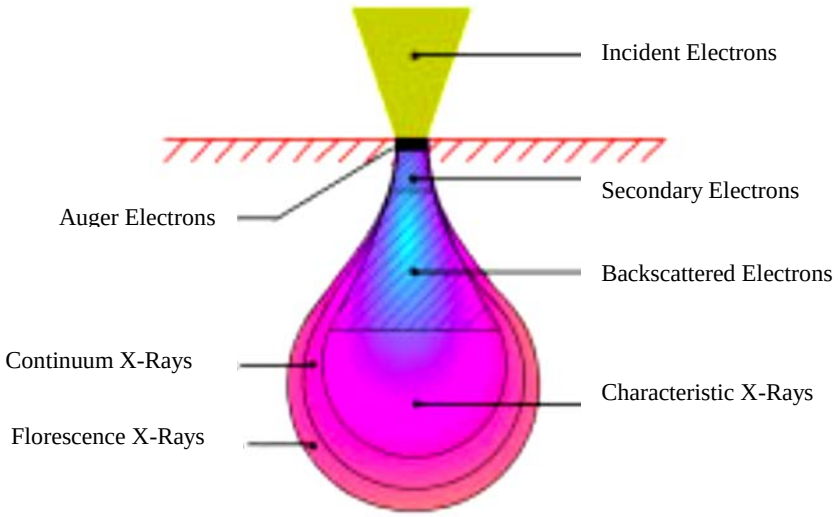

Fig. 15. Interaction volume of different signals generated by an electron beam [67].

8.4 Auger Electron Spectroscopy (AES)

Like the EDX technique, auger electron spectroscopy is used to obtain the elemental composition of a sample. However, AES possesses better resolution than the EDX technique due to the much lower interaction depth of the auger electrons coming from the top atomic surface layers (4- 10 Å). When the electron beam used as a source of energy has sufficient energy, it may remove one electron from the inner shell, and, consequently, one electron from an outer shell will be replaced to make the atom energetically stable. The differences between the energy of these two shells can aid the emission of a third electron called the Auger electron, which contains characteristic information about the material of the sample. To obtain elemental depth profiling, the auger microscope can also be equipped with ion guns.

In the present study, AES analysis was performed by means of a PHI 700 Xi Scanning Auger Nanoprobe with an acceleration voltage of 10 kV and a beam current of 10 nA. Depth profiling was performed with 2 kV Ar+ ion sputtering. The sputter rate was set at 17 nm/min for Ta2O5 using a Ta2O5 reference standard under the same sputtering conditions. Quantitative analyses were conducted using the peak-to-peak height of the Auger transitions of a specific element together with sensitivity factors determined using PHI.

8.5 Manual Cross Section

To obtain an overall view of the oxide scale covering an entire sample, larger cross sections are needed. Samples can be mounted in epoxy before cutting. The procedure can be followed by grinding, polishing, and cleaning of the prepared cross section.

In this study, samples were mounted in epoxy and cut with a saw. The cross sections were then ground with SiC papers to 1000 mesh. Afterwards, they were polished with diamond paste down to 1 µm. The samples were degreased and cleaned with water, acetone, and ethanol using ultrasonic agitation. The sample preparation was performed with a Struers machine. Up to the microscopy time, the samples were stored in a desiccator. It should be noted that the oxide scales of the laboratory exposure samples were not sensitive to any of these cleaning solutions. Although the cross sections were affected by sample preparation, they remained valuable for overall view imaging and EDX analysis.

8.6 Focused Ion Beam (FIB) - FIB/SEM workstation

A FIB can be used both as a microscope (for imaging) and a miller (ion milling to make cross sections). However, it is primarily used for high precision milling to produce smooth sections prior to micro-analysis. In this study, an FEI Versa 3D DualBeam FIB/SEM workstation was used. The machine was equipped with a liquid gallium source and a platinum supplier. Before making the cross sections, a platinum layer was deposited on the area of interest, to protect the surface of the scale, and, finally, the sample was milled with gallium ions. To prevent any redisposition, fine milling was always done at the end of the process. The cross sections were usually between 10 to 40 μm across. The larger the cross section, the more time the process takes both for platinum deposition and ion milling. The drawback of the system is that the sample surface is always affected by ions even in low ion current and low magnification for ion imaging. Another drawback is that the cross section is small compared to the sample size. Thus the FIB technique is more efficient when local corrosion attacks need to be investigated. The advantage of this technique is that a sharp cross section can be provided which is not affected by external factors, e.g., sample preparation process compared to a manual cross section.

8.7 Broad Ion Beam (BIB)

When wide cross sections are needed, the broad ion beam (BIB) technique is more efficient than FIB. It works in a way similar to the FIB technique but instead of gallium, a broad argon ion beam (~1mm) is applied. In this study, some of the cross sections were prepared by means of a Leica EM TIC 3X BIB equipped with three argon sources. Prior to BIB milling, the samples were coated first with Au. Then a very thin glass sheet was stuck onto the sample to protect the top oxide surface further while milling. Finally, the samples were cut with a low speed saw and prepared for the BIB. Especially for the field exposure samples, it was necessary to prepare the cross sections with BIB milling since the samples were sensitive to manual cross-sectional preparation. The samples were covered with a deposit layer which was sensitive to the cleaning solutions. The deposit contained alkali salts which could be easily dissipated by cleaning with solutions containing water. BIB was therefore used to make cross sections of the field samples.

8.8 Transmission Electron Microscopy (TEM)

A high resolution investigation of microstructural features with imaging, in addition to valuable information about the chemistry and crystallography of a sample, makes the transmission electron microscope (TEM) a unique tool. However, in comparison to SEM, the analysis obtained using TEM can be more expensive and time consuming. Precise sample preparation is needed for TEM analysis. The prepared sample has a thin foil with a thickness in the range of 20 to 200 nm. Unlike the SEM discussed above, the micrographs obtained using TEM analysis are based on the detection of electrons transmitted through the thin foil. In other words, a TEM analysis is a result of the interaction of a high energy electron beam with atoms when the beam passes through the thin foil. The high energy electron beam is able to resolve microstructural details at the atomic level. In the present study, an FEI Titan 80-300 TEM/STEM equipped with an Oxford Inca EDX detector was used. STEM images were acquired in HAADF mode. STEM/EDX analysis was performed in order to obtain the chemical composition of small features present in the oxide scale of a sample. The electron energy loss spectroscopy (EELS) technique was only used for qualitative identification of elements.

The TEM analyses were performed by Ph.D. Mohammad Sattari and PhD. Torbjörn Jonsson at the Department of Chemistry and Chemical Engineering, Chalmers University of Technology.

8.9 Oxygen Sensor

In order to measure oxygen partial pressure at various positions in the system, a Rapidox 2100ZF Oxygen analyser was used. This analyser operates in the oxygen range between 10^{-20} ppm to 100% and the accuracy is ± 1% of the actual measured oxygen with a precision of ± 0.5% [68].

8.10 Thermodynamic calculation

The thermodynamic calculations were made by means of the software FactSage using FactPS (Fact Pure Substances) database. In *Papers IV* and *V*, the thermodynamic calculations were performed by Ph.D Torbjörn Jonsson, using the software THERMO-CALC with the database TCFE7.

9 Results and discussion

As mentioned in the introduction, compared to combustion, the available oxygen in the gasification environment is deficient [2] for the complete conversion of hydrocarbons, and the resulting gaseous products are dominated by species like H_2 (g) and CO (g). Currently, low alloy steels and stainless steels are widely used in power plants. The ability of particularly stainless steels to form a thin protective Cr-rich corundum-type oxide makes them a good choice for use in high temperature applications. In order to obtain a general understanding of the corrosion behaviour of materials, a set of exposures was performed in a 2 MW biomass-fired gasifier as a starting point of the present thesis. Due to the complexity of the environment, i.e., that it includes different gases and alkali salts, the second step was to proceed with the corrosion studies in a more simplified and well-controlled environment. As will be shown in the following chapter, the gasifier environments contain considerable levels of H_2 and H_2O. Since these two gases can also be found in other energy systems, such as combustion engines, the anode side of solid oxide fuel cells and steam power plants, the laboratory exposures were mainly focused on environments containing H_2-H_2O.

9.1 Field Exposure (see paper I)

For the field study, two different types of steels were analysed; 304L stainless steel and T22 low alloy steel. The chemical composition of the samples is shown in Table 1. The samples were attached to the probe tip which was connected to a control system and a nitrogen supplier. The gas temperature was between 700-750 °C, and the samples were cooled down to 600 °C by the pressurized nitrogen. The location of the probe is shown in Fig. 10. Table 2 shows the chemical composition of the gas in the exposure area.

Table 2. Gas composition of the gasifier on the probe tip.

Gas composition	**H_2**	N_2	CH_4	CO	CO_2	C_2H_4	C_2H_2	C_2H_6	H_2S	C_3H_x	**H_2O**
Vol-%	**14**	3	6	14.5	10	2	0.24	0.13	0.03	0.11	**50**

The samples were exposed for 4 hours. After the exposure, the surface of each sample was covered with a deposit with a thickness of about 100 μm. In order to obtain a better understanding of the corrosion behaviour of the alloys, the deposit formed on top of the samples was investigated first. An XRD analysis showed that the deposit mainly consisted of carbon=-containing species, K_2SO_4, KCl and ZnS. The presence of zinc species was unexpected considering the fuel and bed material composition. This is suggested to be a result of the presence of impurities in the fuel. Moreover, K_2SO_4 is not thermodynamically stable in this reducing environment. These species can either be formed on the sample as a result of an equilibrium reaction between the gas species and the metal surface, or have entered the exposure area as particles from another part of the system. If the former is the case, it indicates that the deposit is not in equilibrium. However, the present findings do not allow us to draw such a conclusion. Analyses of deposit particles (present in the gas flow) will be performed in future studies. Fig. 16 illustrates how the deposit was spread on the sample surface. The EDX point analysis showed that the bright regions contained more potassium, sulphur, zinc and oxygen than the dark areas.

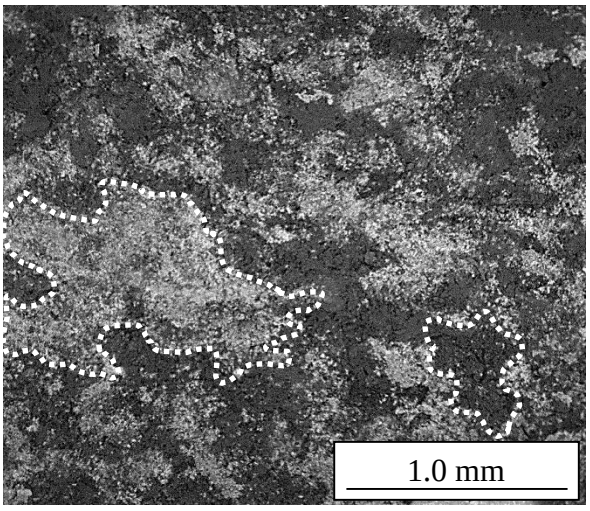

Fig. 16. Plan view BSE image of the deposit formed on top of the 304L (18/10) sample exposed in the gasifier for 4 hours. Examples of bright and dark regions are shown with dotted lines.

Corrosion attack on stainless steel 304L

Fig. 17A shows the plan view BSE image of the 304L sample exposed in the gasifier for 4 hours. The dark region is the area covered by the deposit, and the bright one is the area in which the deposit has been spalled off, making the oxide beneath observable. As can be seen in Fig. 17B, which shows the oxide formed beneath the deposit in higher magnification, the scale mainly consists of two different oxide features; a thin protective oxide and thick oxide islands.

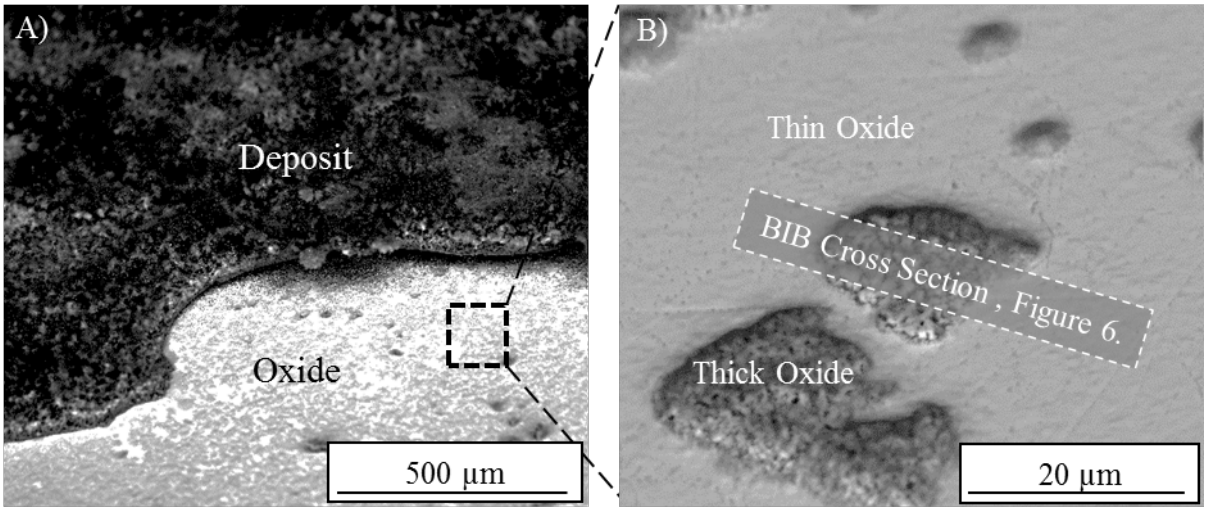

Fig. 17. Plan view BSE image of the 45º-tilted 304L sample exposed in the gasifier for 4 hours. A) The dark region is the area covered by the deposit, and the bright one is the area in which the deposit has been spalled off, making the oxide beneath observable. B) The oxide formed beneath the deposit, which consists of thick and thin oxide layers, at higher magnification. BIB cross section is shown in Fig.6 in *Paper I.*

It has been shown in several studies [48, 69-73] that 304L alloy forms a thin protective Cr-rich corundum-type oxide at high temperatures in a mild environment such as dry oxygen or air. This is in good agreement with the present observations of both the plan view and the cross-section, where the scale is too thin to be observed with SEM/EDX (see Figs. 17-18). However, the oxide scale has lost its protective properties in some areas of the surface, see Fig. 17. This type of oxide scale typically covers 20-50 µm wide sections, i.e. approximately the same size as the alloy grain size [73]. To characterise the corrosion morphology, a cross section of the sample was made by means of Broad Ion Beam (BIB) milling on the thick oxide islands, see Fig. 18. The scale thickness was about 1µm and consisted of two distinct layers; an outward

growing Fe-rich oxide and an inner layer containing Fe, Cr, Ni oxide, see Fig. 20. In the inner layer, different contrasts can be seen in the BSE/SEM image shown in Fig. 19. These are interpreted to be mainly due to a difference in chemical composition. Due to the thin oxide layers and poor resolution of the SEM/EDX analysis, the EDX point analysis was subjected to interactions of several layers. However, the oxide features of the inner layer are in good agreement with the previous study [74], indicating the presence of fully oxidised regions as darker-contrast features and internal oxidation zones as brighter-contrast features. This is due to the presence of Fe,Ni metals adjacent to Fe,Cr oxide nano-particles in a non-fully-oxidised region. This type of corrosion morphology will be discussed in detail in the Section 9.2.6.

In addition, due to the presence of a thick deposit layer on top of the sample and thin oxide features beneath the deposit, it was not possible to resolve the oxide phases by means of XRD. Consequently, a more advanced tool is needed to investigate the exact composition and phase of the oxide layers, e.g., Transmission Electron Microscopy (TEM).

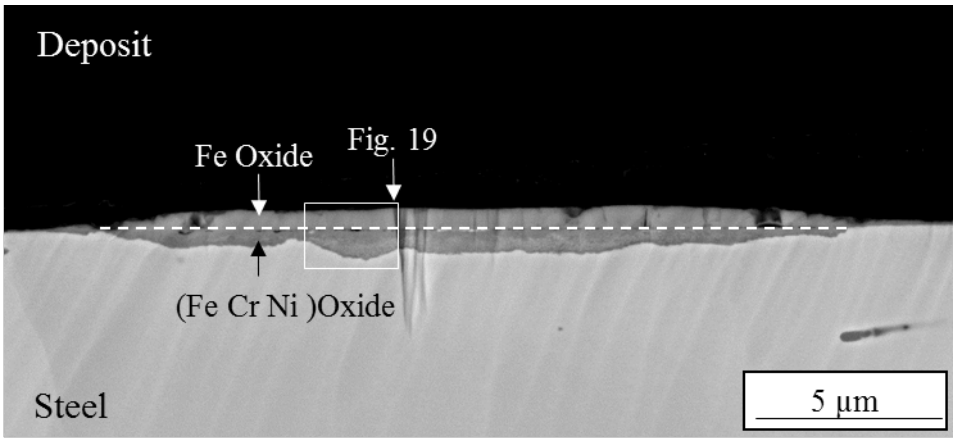

Fig. 18. BIB Cross section of 304L sample exposed in the gasifier for 4 hours at 600 ºC. The sample surface was covered with a thin oxide and a thick oxide. The latter consists of an outward-growing Fe-rich oxide and an inward-growing FeCrNi oxide.

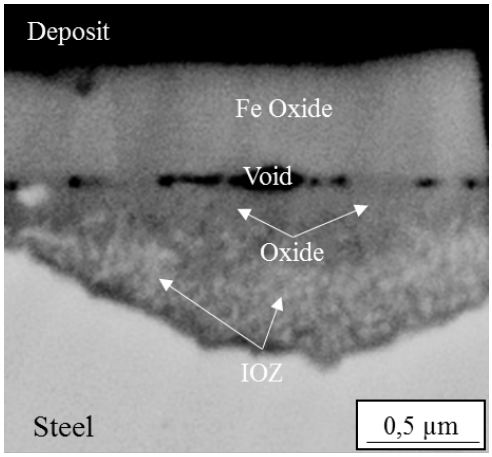

Fig. 19. The region shown in Fig. 18 in higher magnification.

As shown in the figure, the sample had lost its protective properties in some regions even after a short exposure (4 hours). It is expected that this type of oxide morphology does not provide sufficient corrosion protection, and, as a result, the initial corrosion attack can be expected to progress with time. Due to the complexity of the flow gas in addition to the presence of the deposit in direct contact with the alloy, it is hard to describe the main mechanism responsible for the initial corrosion attack. However, some suggestions can be proposed. As mentioned, the deposit consists of some alkali, which has been shown to react with chromium in high oxygen activity. This would deplete the protective scale on the chromium and create a similar microstructure [73]. The high water vapour (about 50 vol%) content in the environment may also explain the breakdown of the protective scale. As in the present study, the breakaway oxidation of stainless steels, because of the presence of either alkali salts or water vapour, has been reported to result in a similar microstructure consisting of an outward growing iron-rich oxide and in inward growing Fe,Cr,(Ni) spinel [27, 37, 40, 73-75]. The microstructure of the inner layer consists of fully oxidised regions as well as regions of internal oxidation [74]. This type of oxide morphology will be discussed in detail in Section 9.2.6.

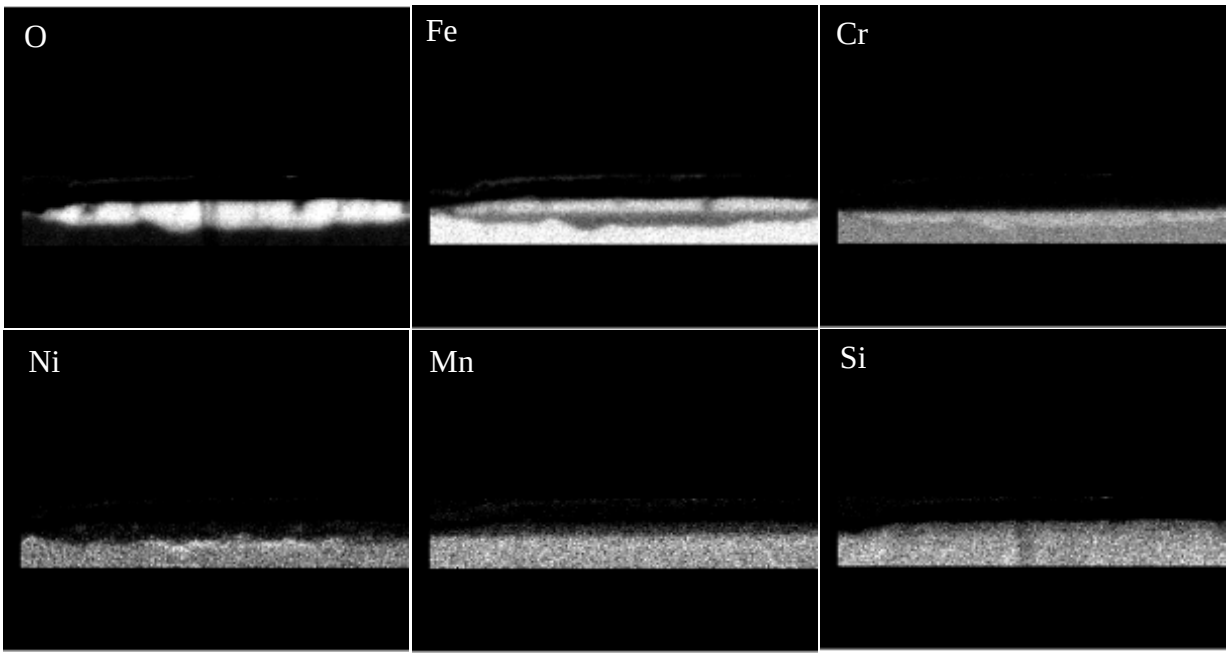

Fig. 20. Cross sectional EDX map of 304L sample exposed in the gasifier for 4 hours at 600 ºC.

Corrosion attack on low alloy steel T22

The initial corrosion attack on the low alloy steel T22 was also investigated in the 2MW Chalmers fired gasifier. However, since this alloy is not the main focus of the thesis, only a brief description of the findings will be discussed below. Further discussion is available in *Paper I.*

A cross section of the low alloy steel T22, from a position similar to the 304L sample, i.e. beneath the deposit, was made by means of BIB, see Fig. 21. The oxide scale consisted of two distinct layers. There was a gap between the layers which had been filled with some impurities from the sample preparation. The outermost layer was about 7 μm and consisted of almost pure iron oxide. The inward growing oxide layer was about 3 μm and contained both Fe and Cr. The thick scales exhibited a sharp straight line in the middle of the scale that separated the bottom spinel oxide from the outer parts of the scale, i.e. the gap. The dark spots in both the inward and outward growing oxides were found to be voids. The inner layer is suggested to be a FeCr spinel-type oxide grown by the inward transport of oxygen ions. The fact that chromium is only present in the inward growing layer is suggested to be explained by the low diffusivity of Cr^{3+} in comparison to Fe^{2+} in spinel oxides [76]. The microstructure formed initially in the gasifier is comparable with the scale formed on a low-alloyed steel under combustion conditions, see

e.g. [77]. As in the case of the 304L alloy, the outward growing layer is suggested to be magnetite due to the low partial pressure of oxygen.

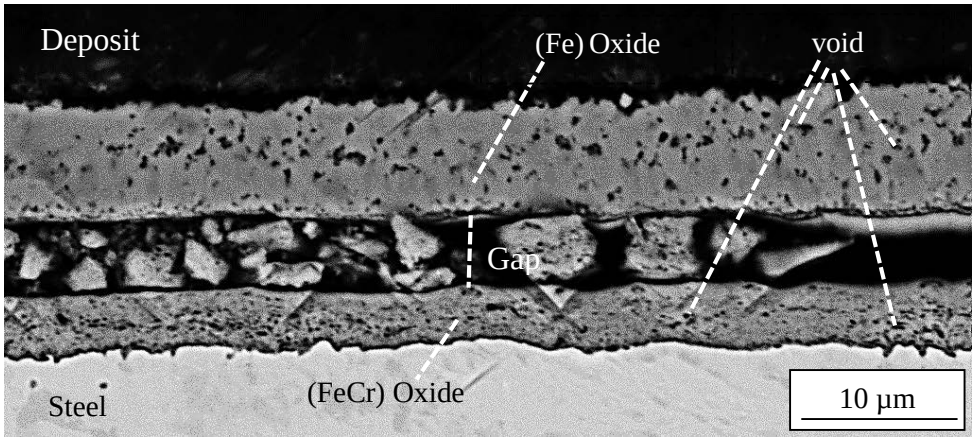

Fig. 21. BIB Cross section of T22 sample exposed in the gasifier for 4 hours at 600 ºC.

The oxide thickness of this sample is about 10 µm, which is about 10 times greater than the oxide thickness of the 304L samples. This means that the initial corrosion attack was less on the stainless steel than on the low-alloy steel in the gasifier. This is due to the lower Cr content of T22 than 304L, which makes the alloy unable to show proper protective properties towards corrosive environments.

Thus, it can be concluded that both of these materials suffer initially from a corrosion attack in this corrosive environment. However, the main mechanism responsible for the initiation of the corrosion in this complex environment is not still clear. Therefore, it was decided to simplify the environment in order to obtain a better understanding of the corrosion behaviour of these materials in a gasifier environment. As shown in Table 2, the environment contains considerable amounts of H_2 and H_2O. Since H_2 and H_2O can be found in many energy systems, such as combustion engines, the anode side of solid oxide fuel cells and steam power plants as well as gasifiers, laboratory exposures should mainly focus on environments containing H_2 and H_2O as a first step. In future research, a study of this type will be conducted by adding the other gas species and salts to the environment.

Although it was shown that even 304L stainless steel suffers initially from a corrosion attack in this corrosive environment, it was selected as the main material for the laboratory studies of

this thesis. This is due to the fact that this material is often used as a reference for corrosion exposures.

9.2 Laboratory exposures

The main focus of the laboratory exposures was on the oxidation behaviour of 304L in environments containing H_2 and H_2O for the reason described above. The effect of these gases will be discussed in detail in the following sections. However, prior to starting the main exposures and because of the importance of good control over the experimental process, it was essential to do a ‘’process investigation’’ for the corrosion experiments in low $a(O_2)$ environments. In high $a(O_2)$ environments, the oxygen impurities available in the experiment chamber (resulting from e.g. the carrier gas and leakages) are not expected to affect the corrosion results considerably during exposures. But the effect may be significant on the oxidation behaviour of steels in low $a(O_2)$ environments, like the studied environments in the present work.

The main purpose of the ‘’process investigation’’ was to show how important it is to have good control of the exposure environment, not only during the exposure but also during ramping the furnace up and down. Since hematite is not thermodynamically stable at oxygen activities below about 10^{-16} (at 600 °C), hematite formation and the use of a sensitive oxygen analyser [68] for $a(O_2)$ measurements were considered as a quality check of the process here.

9.2.1 Process investigation (*see Paper II*)

As mentioned above, more focus is necessary for exposures in low $a(O_2)$ than in high $a(O_2)$ environments. This is due to the fact that oxygen impurities (even in ppm ranges) have a great influence on gas-phase chemistry, which affects equilibrium in low oxygen activity exposures, e.g., H_2/H_2O mixtures. This effect is more pronounced when exposures are performed in pure steam or Ar-H_2O.

However, when a few percentages of hydrogen are also present in the environment, e.g., in Ar-H_2-H_2O system), the effect of impurities becomes negligible. In this case, hydrogen and oxygen impurities react at high temperatures, and , thus, the role of the oxygen impurities of the carrier gas becomes insignificant on the overall equilibrium oxygen activity of the environment [78].

Therefore, it can be assumed that the effect of Ar (as a carrier gas) flask impurities would be negligible in the present work during the main exposures, i.e., in an H_2-H_2O-Ar environment at 600 ºC. However, since the overall time needed for heating-up and cooling-down the furnace is considerable, the effect of impurities during these sequences also needs to be investigated. It

is generally believed that flushing the chamber with high purity argon gas prior to exposures in low a(O_2) environments is sufficient to suppress the formation of unwanted reactions. But, as discussed above, even today's high quality Ar flasks contain some impurities, e.g., oxygen, see Table 3, which can affect the gas equilibrium in the exposure chamber during the ramping up/down sequences.

Table 3. Impurities available in a high quality Ar flask with purity ≥ 99.9999%

O_2	H_2O	C_nH_m	CO	CO_2	H_2	halocarbons
≤ 30 ppb	≤ 50 ppb	≤ 30 ppb	≤ 30 ppb	≤ 30 ppb	≤ 30 ppb	≤ 1 ppb

To address the importance of the presence of these impurities during the exposure, 304L samples were exposed to Ar- 10 % H_2- X% H_2O (X= 2, 20, 50) for 24 and 72 hours. The exposures were started by placing the samples in a cold furnace. The samples inside the sealed alumina tube were flushed with Ar for 24 hours in order to remove any residual air. After this flushing period, the temperature in the furnace was set to 600 °C. With a temperature ramp of about 15 °C/min, the desired exposure temperature, i.e., 600 °C, was reached after approximately 40 minutes while flushing with pure Ar. Once the temperature of the furnace reached 600 °C, the gas mix was switched to the intended gas mixture, i.e., 10% H_2- X% H_2O-Ar. After the intended exposure time (24 or 72 hours), the furnace was switched off with a continuous flow of pure Ar. The cooling down period lasted for about 9 hours in order to reach room temperature. Consequently, it cannot be assumed that the share of the total time allocated by the start-up and ending sequences is negligible, especially for a short time exposure.

The XRD analysis showed that the corrosion products mainly consisted of hematite (Fe_2O_3) and spinel-type oxide for all the exposed samples, see Fig. 22. However, the calculated and measured oxygen activity of the environments (Ar-10% H_2-X% H_2O) at 600 ºC were in the range of about 10^{-23}-10^{-26} bar, which is far less than the oxygen dissociation pressure needed for the formation of hematite. Thus, it is assumed that hematite might have been formed during the ramping up and down sequences instead, while the furnace was being flushed with Ar.

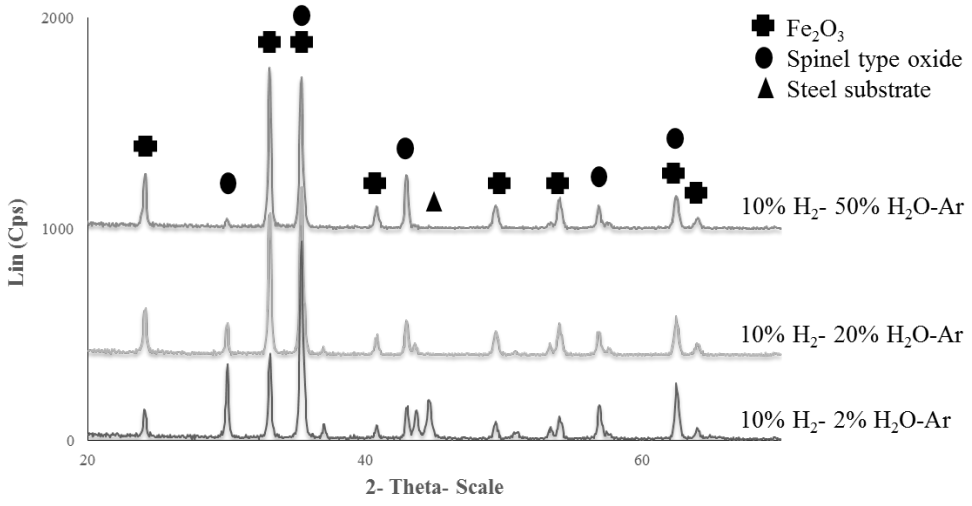

Fig. 22. Crystalline phases detected with XRD on 304L samples exposed at 600 °C for 72 hours in 3 different environments.

In order to determine if the hematite had formed during ramping up or down, the system was checked for a shorter exposure time (4 hours) using Ar, Ar + 10% H_2 and Ar +10% H_2 + 20 % H_2O as the flushing gases during the start-up and ending sequences, respectively. The main exposure, i.e., during the 4 hours, was performed in an Ar+10% H_2 + 20 % H_2O environment at 600 ºC for all the tests.

9.2.1.1 Ar used as gas during start-up and ending sequences

The formation of hematite was detected (see *P*aper I) when Ar was used during the start-up and ending sequences. A detailed investigation of the system by means of the oxygen sensor, showed that a(O_2) drops dramatically during the heating up till 600 ºC while the samples were inside the furnace. Therefore it is suggested that the oxygen impurities inside the chamber are consumed by the steel for the oxidation reaction and thus lead to hematite formation. This suggestion is further supported by the results showing that no changes in a(O_2) occurred when no sample was inside the chamber.

In order to minimize the effect of oxygen impurities, 10% H_2 was added to the Ar during the start-up and ending sequences.

9.2.1.2 10% H_2 + Ar used as gas during start-up and ending sequences

XRD analysis showed that when 10% H_2 + Ar was used as a flushing gas, hematite formation was hindered and the scale only consisted of spinel-type oxides. However, since the 10% H_2 + Ar provides a highly reducing environment, the spinel-type oxide formed during the main exposure, i.e. during the 4 hours, may also be reduced during the ending sequence. Thus, in order to optimise the process, a mixture of H_2/H_2O was used during the start-up and ending sequences as the next step.

9.2.1.3 10% H_2 + 20% H_2O Ar used as gas during start-up and ending sequences

Similar to the 10% H_2 + Ar test, no hematite formation was observed when 10% H_2 + 20% H_2O + Ar were used as the gas mixture during the start-up and ending sequences. However, the mass gain of the 304L samples used in the latter case was about two times higher, indicating that the spinel-type oxide formed during exposure was reduced to metallic iron in the 10% H_2 + Ar exposure.

Thus, as discussed, conducting exposures in low oxygen activity environments demands good control of the system. To provide a low oxygen partial pressure environment and to avoid the formation of unexpected oxide layers caused by impurities entering the system, e.g., via carrier gas bottles and small leakages in the system, precise control of the exposure is needed. It is important to ensure that, not only during the exposure but also during the start-up and ending of the exposure, the environment maintains a low oxygen partial pressure.

For the rest of the study, the exposure process as described in Section 9. 1. 1. 3 was followed, i.e., during the start-up and ending sequence; the system was flushed with the same gas composition used during the main exposure time.

9.2.2 Effect of H_2, H_2O, and a(O_2) (see *Paper III*)

Before conducting a detailed study of the oxidation mechanism in the presence of H_2 and H_2O, the general effect of each of these gases was investigated separately. A comprehensive results and discussion section has been provided in *Paper III*. Below is a brief summary of those observations.

The 304L samples exposed at 600 ^oC for 24 and 72 hours in H_2-H_2O-Ar with various gas mixtures;

- First, in order to determine the effect of water vapour, the H_2 level of the environment was kept constant at 10 vol% and the H_2O level was varied from 2 vol% to 50 vol%.
- Second, to see the effect of H_2, the H_2O level was fixed at 20 vol% and the H_2 level changed from 2 vol% to 20 vol%.
- Finally, to keep the a(O_2) constant, H_2 and H_2O levels were changed simultaneously to maintain a fixed H_2/H_2O ratio.

In all the H_2-H_2O environments, the 304L samples suffered from accelerated corrosion compared to the reference exposure performed in dry O_2 at 600 ^oC. In the latter environment, the low mass gain of the samples, even after 72 hours, indicated the presence of a thin protective oxide. However, in the low a(O_2) environments, a thick scale was formed after breakaway oxidation at the alloy/gas interface consisting of an outward-growing Fe_3O_4 and an inner layer containing $(Fe,Cr)_3O_4$ in the form of both fully oxidised regions and internal oxides, in addition to Fe,Ni metal particles. This accelerated attack may have been influenced by the following effects:

- The effect of H_2O content,
- The effect of H_2 content,
- The effect of aO_2,
- The effect of oxide grain size, i.e., grain boundaries density,
- Surface reactions as the rate determining step (e.g. $H_2O \rightarrow OH^-$),

The gravimetry results indicated that the effect of H_2O was more pronounced than the effect of H_2 and a(O_2) on the oxidation rate of the 304L samples at 600 ^oC. The mass gain of the sample exposed to 10% H_2- 50% H_2O- Ar was about 6 times higher than the mass gain of the corresponding sample exposed to 10% H_2 + 2% H_2O. At a fixed H_2O level, slight differences in the oxidation rate were observed when the H_2 content of the environment changed. However,

the environment with the lowest H_2 content, i.e., 2% H_2 + 20% H_2O, exhibited a higher mass gain than those with 10% and 20% H_2. Finally, at a fixed H_2/H_2O ratio, the mass gain increased with an increase in gas levels.

The slope of the mass gain curves from 24 hours to 72 hours, see Fig. 23, was similar for all cases. This indicates that the oxidation kinetics for all the environments in this time period is almost identical (with the exception of the samples exposed to 10% H_2 + 2% H_2O where the oxidation rate was slightly lower). This may suggest that the corrosion product layers formed after 24 hours on the different samples possess roughly the same corrosion resistance. In addition, a microstructural investigation of oxide surface showed that the oxide (Fe_3O_4) grain size varied from one environment to another (compare Figures 2 and 8 in *Paper III*). These two observations would suggest that the oxidation kinetics of the samples have little correlation with the number of oxide grain boundaries, i.e., the rate determining step in the corrosion attack does not seem to be connected to diffusivity through the iron oxide scale. The diffusion through the oxide lattice is expected to be negligible at this temperature. Instead, the findings indicate that the rate-determining step in the corrosion attack is surface-controlled or diffusion-controlled through an oxide layer with a fixed thickness over time, e.g., the initially formed thin Cr-rich scale. However, these findings are only indicative and in order to verify them, more exposures with different exposures times are needed.

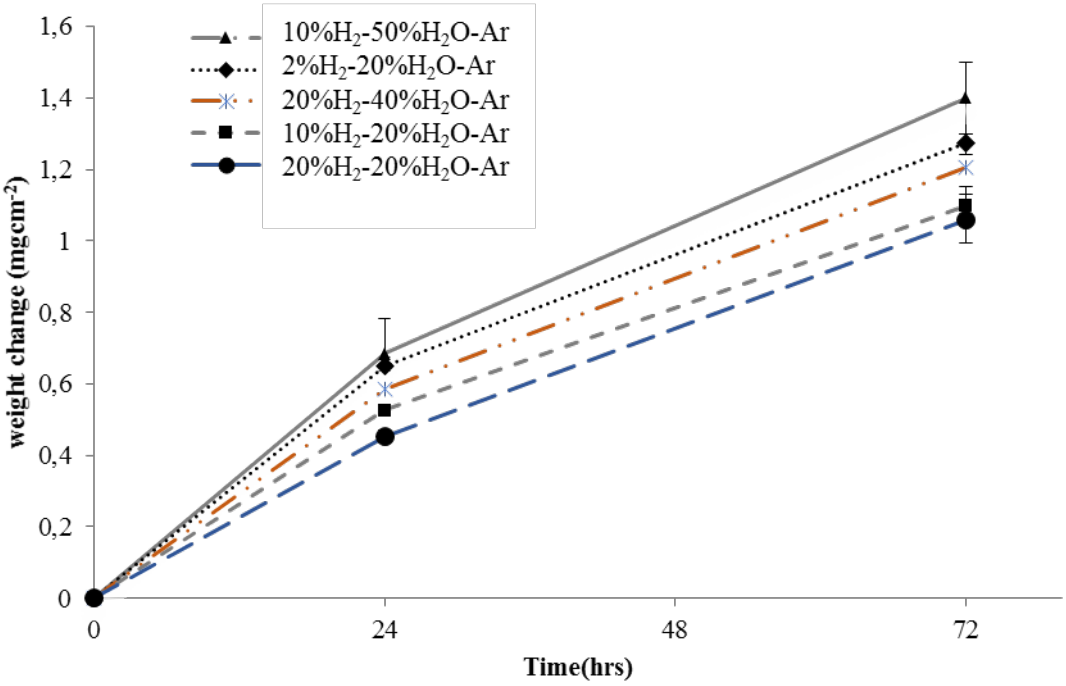

Fig. 23. Mass change versus exposure time for 304L samples exposed at 600 °C.

9.2.3 Initial oxidation after 1 hour (see *Papers III and VII*)

In order to capture the onset of corrosion in H_2-H_2O containing environments, a set of 304L samples was exposed in 10% H_2- 20% H_2O-Ar at 600 ºC for 1 hour. Most of the sample surface was covered with an oxide with a thickness of about 2 µm. However, there were still some regions where the sample was covered by a thin scale, see Fig. 24. An AES analysis was performed on the three different positions shown with dashed lines in Fig. 24 (for the AES analysis see *Paper III*). The analysis revealed that the thin oxide (about 80 nm according to the auger analysis) was chromium rich, the Cr content being 70-80% (cationic percent) with the exception of the top 5 nm where the Fe/Cr ratio reached unity. The high Cr content in the thin oxide suggests that the oxide is a Cr-rich corundum-type oxide. Such an oxide has been shown in previous studies [70, 72, 75, 79] to form on 304L alloys in mild environments, such as dry oxygen or air. The oxide in those mild environments displays a protective behaviour and protects the material from further corrosion. But this is not the case in the present environment. The auger analysis through the dashed line C-D (see *Paper III*) indicated that the oxide had started to grow. The oxide layer in this area could be divided into two parts; the top layer (roughly 70nm in thickness) consists of iron oxide whereas the bottom layer is chromium rich (roughly 100 nm in thickness). The thickness and composition of the bottom layer is similar to the adjacent thin oxide described above. Therefore, it is suggested that the bottom part of the oxide is also a Cr-rich corundum-type oxide. It should be noted that due to the low spatial and depth resolution of the AES analysis, the exact composition of the thin oxide layers is hard to obtain. Thus, in order to achieve better resolution, a TEM sample was prepared from a region similar to the one shown in Fig. 24. The STEM/EDX line scans (see *Paper VII*) showed that the Cr content of the subscale of the thin oxide was about 95 cat.%, i.e., relatively pure chromia.

The AES analysis of the thick oxide region (dashed line C-D) showed the continuation of the oxide growth which led to the formation of an outward growing iron oxide and inward growing oxide layer (see *Paper III*). This type of corrosion morphology can be also seen on samples exposed for 24, 72, and 168 hours, which will be discussed below. Thus, it can be suggested that the corrosion attack in 10% H_2- 20% H_2O- Ar was initiated during the first hour of exposure and continued with time. The XRD findings show that the outward growing layer is Fe_3O_4, which complies well with the low oxygen activity of the environment.

It is important to note that by comparing the results driven from the thin oxide (the dashed line A-B) towards the thick oxide (the dashed line E-F), it can be suggested that; a relatively pure chromia formation on top of the alloy occurs at the initial stage of the oxidation process. This

is followed by an outward diffusion of iron ions that form a magnetite on top of the scale despite the presence of the thin Cr-rich subscale. The scale continues to grow and results in an outward growing magnetite and inward growing oxide.

However, the Cr-rich oxide and the inward-growing oxide layer were not detected with the AES analysis of the region E-F. This can be due to the low resolution of AES analysis. In order to support this theory, a detailed microscopy analysis with higher resolution was performed on 304L samples exposed under the same conditions for 72 hours.

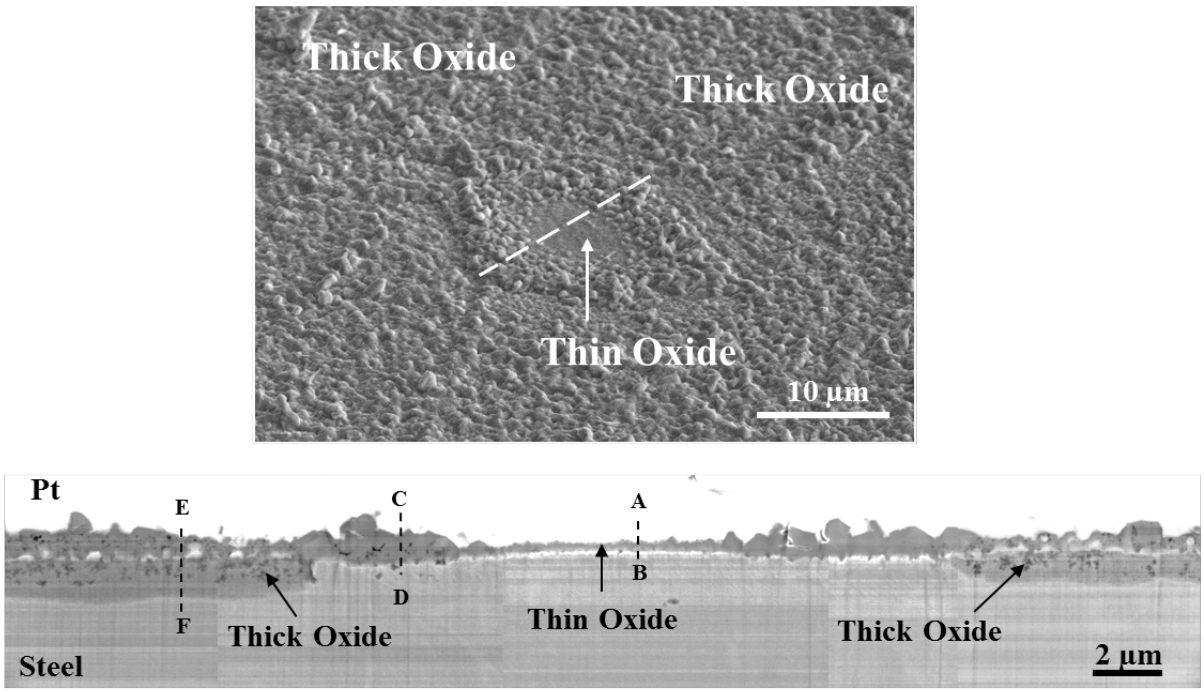

Fig. 24. 304L exposed to 10% H_2- 20% H_2O- Ar at 600 ºC for 1 hour. The majority of the surface is covered with corrosion products, i.e thick oxide. A cross section was performed on an area where a thin oxide was still present (shown with a white dashed line).

9.2.4 Oxidation after 72 hours (see *Paper IV*)

In order to see the footprint of the initial Cr-rich oxide after a longer exposure, the 304L samples were exposed to 10% H_2- 20% H_2O-Ar at 600 ºC for 72 hours. The scale thickness of the

samples was about 15-20 µm. As in the 1 hour exposure, the scale consisted of two distinct layers; an outward growing magnetite and an inner oxide layer, Fig. 25a. However, unlike the one hour sample, the sample surface was totally covered with a thick scale and no areas with a thin oxide were seen after 72 hours.

The STEM image in Fig. 25b is a close-up of the central part of the scale of the sample exposed for 72 hours, including the interface between the inward- and outward-growing oxides. The EDX analysis through line A-B reveals that a 40-50 nm oxide layer with about 55 % Cr and 45 % Fe (cationic) is sandwiched between the iron-rich oxide (outward growing layer) and the Ni-rich zone. This feature is interpreted as a remnant of the initial oxide formed on the original metal surface.

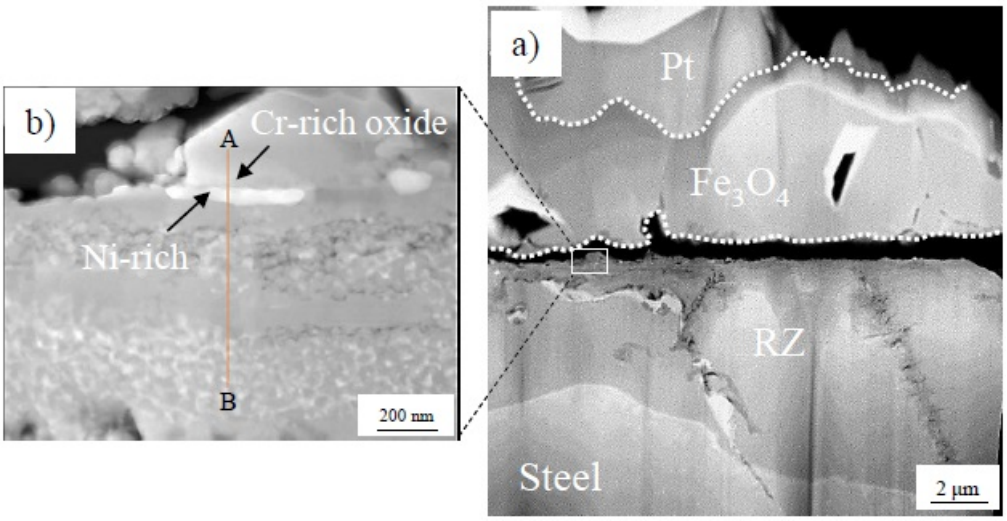

Fig. 25. a) Scanning transmission electron microscope (STEM) high angle annular dark field (HAADF) cross section image of the 304L sample exposed at 600 °C to 10 % H_2-20% H_2O-Ar for 72 hours. b) a close-up of the interface region between the inward and outward growing oxide.

Thus, by comparing Fig. 24 and Fig. 25, it is suggested that the thin (relatively) pure chromia (see Fig.4 in *Paper VII*) is formed during the initial stage of the oxidation process when 304L is exposed to 10% H_2- 20% H_2O-Ar at 600 ºC. As the breakaway oxidation occurs, the process is followed by an outward diffusion of iron ions and inward diffusion of oxidant species, despite the presence of the Cr-rich oxide at the initial metal interface. The oxidation process continues with time and leads to a thickening of both outward- and inward-growing oxide layers. But what is the mechanism responsible for the breakaway oxidation in this environment?

As discussed earlier, it is known that the Cr-rich $(Fe_xCr_{1-x})_2O_3$ that forms on top of the 304L alloy is regarded as a protective oxide layer which suppresses further corrosion of the material in mild environments, e.g., in dry O_2. When a considerable amount of H_2O is also present in a high $a(O_2)$ environment, e.g., in O_2 + H_2O, the oxide is depleted in chromium due to the formation of Cr volatile species e.g. $CrO_2(OH)_2$ (g). This means that the Cr-rich and protective oxide is being transformed into a Fe-rich and poorly protective oxide, and, thereby, the oxide loses its protective properties and results in accelerated corrosion [39, 47]. However, this is not the case in low $a(O_2)$ environments. The partial pressure of volatile Cr species is minor in low $a(O_2)$ environments [80], and the volatilisation of Cr species has a negligible effect on the oxidation behaviour of Cr-containing alloys. Thus, Cr volatilisation cannot be regarded as the main reason for the breakaway oxidation in the present work. In order to further elucidate the effect of H_2O and, consequently, to find the breakaway mechanism in a low $a(O_2)$ environment, the effect of pre-oxidation in O_2 was investigated and is reported on the next section.

9.2.5 Effect of pre-oxidation (see *Paper IV*)

As discussed in the previous sections, a Cr-rich oxide (relatively pure chromia) forms at the initial stage of oxidation when 304L is exposed to 10% H_2- 20% H_2O-Ar at 600 ºC. However, the oxide is not able to protect the alloy from further oxidation. In order to compare the thin oxide formed in dry O_2 and in an 10% H_2- 20% H_2O-Ar environment at 600 ºC, and also to follow up changes that occur in the Cr-rich oxide layer, in addition to the steel substrate beneath the oxide during exposure to H_2-H_2O environments, the samples were first pre-oxidised in dry O_2 at 600 ºC and then exposed to 10% H_2- 20% H_2O-Ar at 600 ºC for 1, 24, and 72 hours. Slowing down the oxidation rate by the pre-oxidation of the sample can enable a better understanding of the oxidation behaviour of the sample in H_2- H_2O environments.

Because of the major influence of pre-oxidation in 5% O_2- 95% N_2 on the oxidation behaviour of alloy 304L in 10% H_2- 20% H_2O- Ar, it was interesting to investigate the microstructure of the oxide formed during pre-oxidation first.

A SEM/SE image of alloy 304L after 24 hours exposure to 5% O_2- 95% N_2 at 600 °C is shown in Fig. 26. At this stage, the alloy surface is covered with a continuous oxide layer with a thickness in the range of 20 -60 nm. The STEM/EDX analysis was performed in two regions (I and II) shown in Fig. 26b (see *Paper IV* for the EDX analysis). In both regions, the oxide had a layered structure, consisting of Fe,Cr corundum-type oxide (with about 70-75 cat.% Cr) at

the bottom and Fe,Cr,Mn spinel-type oxide on the top layers (indications from TEM and XRD results). In both regions, the alloy substrate beneath the oxide was depleted in Cr. The depletion zone was about 60-70 nm and the Cr content was about 1/3 Cr content of the alloy.

This oxide is known as a slow-growing, continuous, adherent, and protective oxide in dry oxygen. This behaviour is well-documented for austenitic FeCrNi alloys and ferritic FeCr alloys at 600°C and 700°C in O_2 and air, and several authors have investigated the oxide scales formed [27, 35, 39, 70, 81].

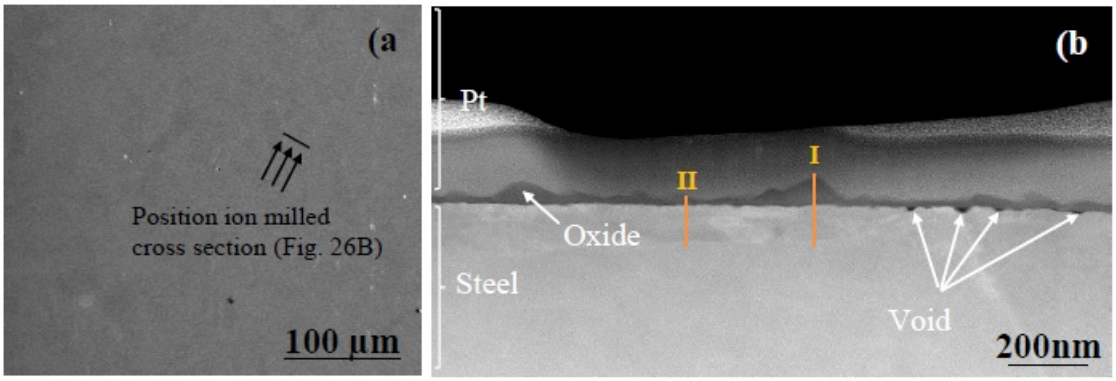

Fig. 26. Scanning Electron Microscope (SEM) secondary electron image of alloy 304L after 24h exposure to 5% O_2- 95% N_2 at 600°C: a) Plan view image b) Cross section image.

After being pre-oxidized in dry O_2, the samples were exposed to 10% H_2- 20% H_2O-Ar at 600 °C for 1, 24, and 72 hours. The results (see *Paper* IV) show that the samples exhibited protective behaviour up till 1 hour. Even after 24 hours, most pre-oxidised samples exhibited mass gains that were comparable to the samples exposed to 5% O_2- 95% N_2, indicating a protective behaviour. Occasionally, relatively large mass gains were observed after 24 hours. After 72 hours in a 10% H_2 + 20% H_2O + Ar environment, all pre-oxidised samples exhibited relatively high mass gains. However, the mass gains were still not as high as for the non-pre-oxidised samples in the same environment. These findings suggest that the Cr-rich oxide, which shows protective behaviour in dry O_2, cannot withstand further oxidation in the H_2-H_2O environment for a long time. However, breakaway oxidation occurs in the pre-oxidised samples after an incubation period. In other words, it takes some time until the protective properties of the thin oxide disappear. But what is the time-consuming breakaway mechanism for the pre-oxidised samples?

In order to answer this question, the pre-oxidised sample exposed to 10% H_2- 20% H_2O-Ar at 600 ºC for 72 hours was investigated by means of Transmission Electron Microscopy (TEM). Most of the sample surface was covered with a thick oxide scale and the thin protective oxides remained intact on just a small fraction of the surface. A cross section of the sample, including both the thin and thick oxides, was prepared by means of FIB milling, and a STEM/EDX line analysis was performed in various regions, see Fig. 27.

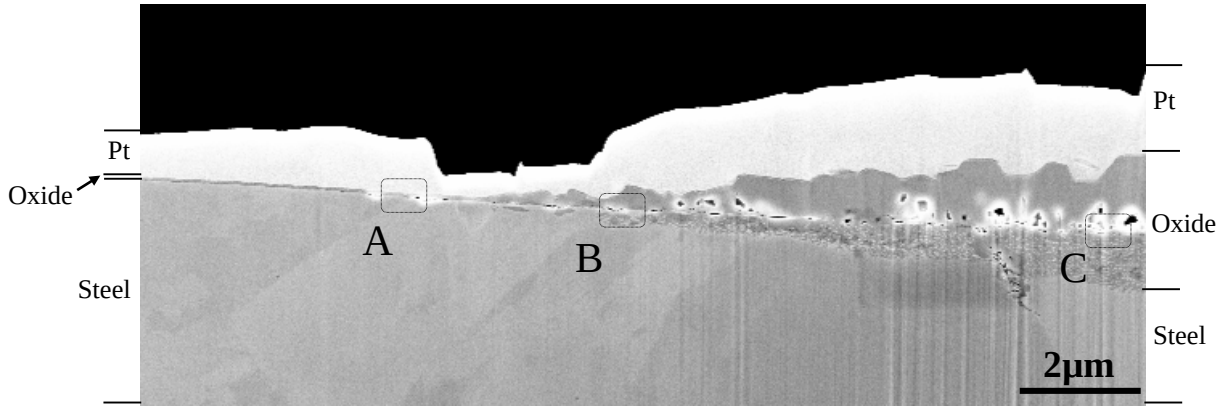

Fig. 27. SE/SEM cross sectional view image of 304L peroxidised sample (in 5% O_2- 95 % N_2) exposed to 10% H_2- 20% H_2- Ar for 72 hours.

Stage I the breakaway mechanism of pre-oxidised samples The EDX analysis in the still protective region, i.e., the thin oxide in region A, revealed that the initial $(Fe_x,Cr_{1-x})_2O_3$ sub-layer formed in the pre-oxidation process, was enriched in chromium and transformed to almost pure Cr_2O_3 (see *Paper IV* for all the STEM/EDX analyses). In addition, the Cr-depletion zone in the alloy substrate beneath the oxide was thicker and contained less Cr (about 2 at.%) after exposure to H_2-H_2O (about 100 nm) than just after the pre-oxidation period (about 60-70 nm with about 6-7 at.% Cr).

Regions B and C show the oxide microstructure after breakaway oxidation. The microstructure of the oxide in region C is very similar to that of the non-pre-oxidised sample shown in Fig. 25b (compare Figures 3b and 14 in *Paper IV*). The discussion regarding the propagation step, i.e., regions B and C in Fig. 27, will be provided in the following section. However, it is interesting to mention here that the STEM/EDX analysis indicated the presence of Cr-rich oxide at the initial alloy interface even after breakaway oxidation, i.e., in the regions B and C. In other words, the outward diffusion of iron ions, in addition to the inward diffusion of oxidant species,

occurs despite the presence of the Cr-rich oxide. However, as mentioned earlier, the chemical composition of the thin oxide and the alloy substrate beneath that oxide just before the occurrence of breakaway oxidation is different from those of the pre-oxidised samples. But what are the reasons behind these changes in the thin oxide and the alloy beneath that oxide before and after oxidising in H_2-H_2O?

Two main reasons can be suggested for the observed differences. The first suggestion is that when the $(Fe_x,Cr_{1-x})_2O_3$ layer is exposed to a low $a(O_2)$ environment, the iron oxide, which is not thermodynamically stable, is reduced. This leads to the formation of metallic iron and leaves behind pure Cr_2O_3. This was observed in Region I in *Paper IV* where the top 20nm of the substrate partly consisted of metallic iron generated by the reduction of iron oxide in the scale. The second suggestion is that since $(Fe_x,Cr_{1-x})_2O_3$ is not thermodynamically stable in the present low $a(O_2)$ environment, it decomposes to Cr_2O_3 and FeCr spinel oxide. For instance, if the $(Fe_x,Cr_{1-x})_2O_3$ formed after preoxidation contains 70 cat.% Cr, based on thermodynamics, it decomposes to pure chromia and FeCr spinel oxide when exposed to 10% H_2- 20% H_2O- Ar at 600 ˚C, see Fig. 28. It should be noted that this is not the case in high $a(O_2)$ environments, e.g., dry O_2, in which $(Fe_x,Cr_{1-x})_2O_3$ is stable with a Cr content in the range of 0-100 cat.%.

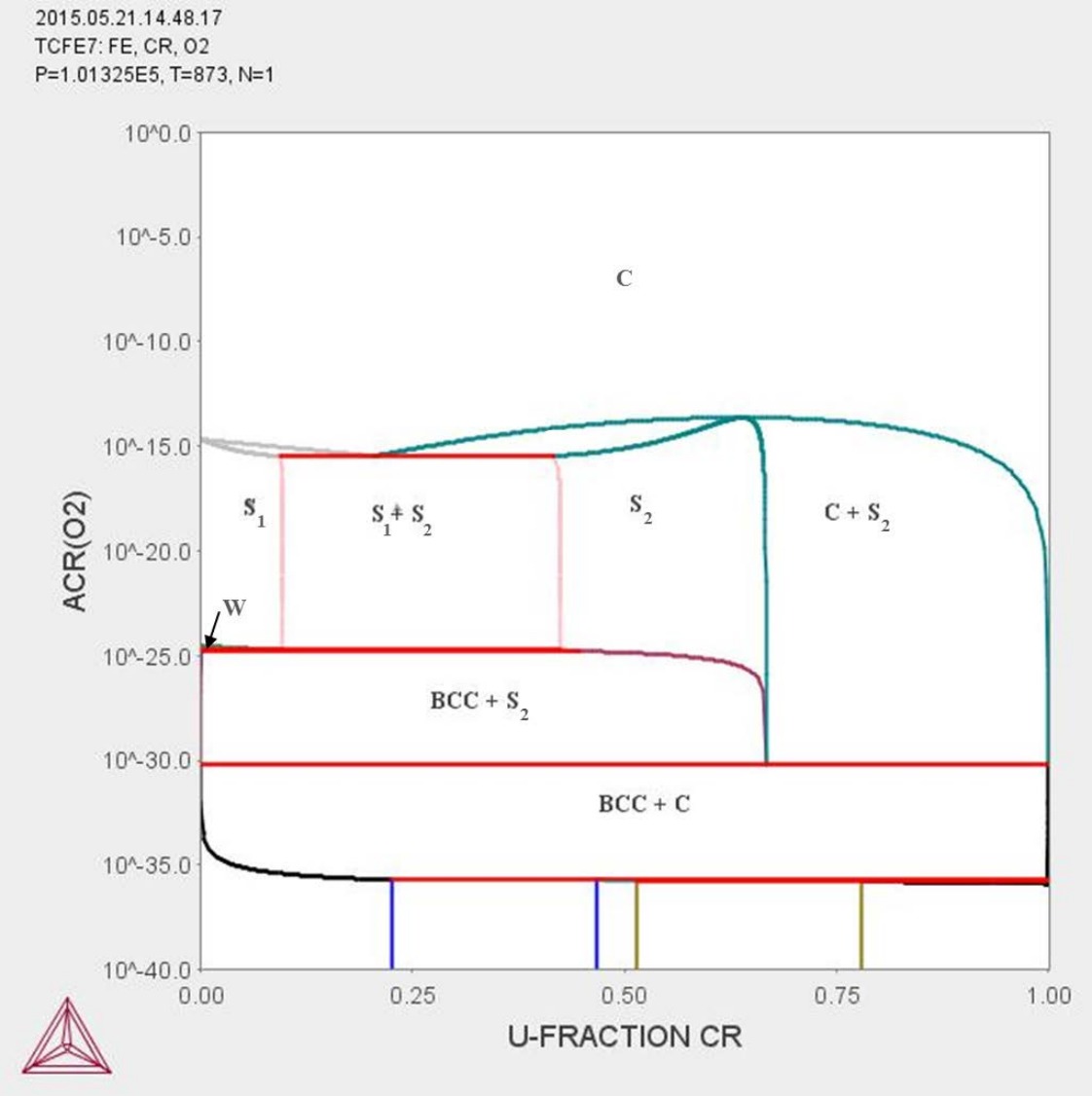

Fig. 28. Stable phases in the Fe-Cr-O system at 600 ºC as a function of oxygen activity and mole fraction of Cr calculated using the THERM-CALC program [82] with the database TCFE7. C = corundum-type M_2O_3 , S_1 = $Fe_{3-x}Cr_xO_4$, S_2= $FeCr_{2-x}Fe_xO_4$, W= $Fe_{1-x}O$, BCC = ferrite-structured metal.

Stage II the breakaway mechanism of pre-oxidised samples The strongly sub-parabolic oxidation kinetics observed for alloy 304L in O_2 at 600 ºC (see Fig. 1 in *Paper IV*) is in agreement with several reports on FeCr and FeCrNi oxidation in air and in dry O_2. Pujilaksono et al. [27] have reported that oxidation of binary FeCr alloys in dry O_2 at 600 ºC results in almost step-like mass gain curves with very little oxide growth after 1 hour . In contrast, the oxidation of pure chromium has been reported to follow approximately parabolic kinetics under the same conditions [83]. In addition, a 24h exposure to dry O_2 at 600ºC has been reported to result in much thicker oxide scale growth on pure Cr than on Fe10Cr, Fe18Cr,

Fe25Cr, 304L and 310 [27, 37, 70, 84]. It is suggested that the deep Cr depletion of the substrate of the pre-oxidized material in an $H_2 + H_2O + Ar$ environment is caused by the replacement of the $(Cr_{1-x}Fe_x)_2O_3$ present at the bottom of the scale, after pre-oxidation in O_2, by Cr_2O_3. Thus, the change in oxide composition results in an increase in the growth rate of the external scale and a correspondingly higher and deeper depletion of Cr in the alloy (see Figs. 9 and 10 in *Paper IV*).

Stage III ***the breakaway mechanism of pre-oxidised samples*** As the alloy becomes Cr depleted (by the growth of Cr_2O_3), the oxygen activity at the alloy substrate beneath the thin oxide increases and eventually becomes high enough for iron to be oxidized. At this stage, a second condition for the outward diffusion of iron ions should be also considered. It is suggested that Cr-rich corundum-type oxide is permeable to outward diffusion of divalent cations via grain boundary diffusion. This has been reported by Canovic et al. [85] who have shown the outward diffusion of Mn^{2+} through the Cr_2O_3 layer at 850 ^oC. Thus the oxidation process in the present case is suggested to be followed by the outward diffusion of Fe^{2+} through the formed Cr_2O_3 layer after oxidising in the H_2-H_2O environment, resulting in the formation of Fe_3O_4 on top of the thin oxide.

Stage IV ***the breakaway mechanism of pre-oxidised samples*** The oxidation continues by inward diffusion of oxidant species and the formation of reaction zone, i.e., an inward-growing layer consisting of a relatively small fraction of fully oxidised FeCr spinel regions and a large fraction of internal FeCr oxides, leaving Fe,Ni metal particles behind [74]. The oxidant species may penetrate through the scale in different forms, e.g., following the Wagner-type oxidation theory in the form of OH^- [41, 45] or transport of water via grain boundaries [86]. It is suggested that in the present case, water vapour penetrates through the scale in a way similar to the one described by Lindgren et al [86]. It is proposed that water hydroxylate the oxide grain boundaries and reach the oxide metal interface. As water comes into contact with metal it reacts:

$$H_2O(GB) + M(metal) \rightarrow MO(s) + 2H(alloy) \quad (15)$$

Or:

$$H_2O(GB) \rightarrow O(alloy) + 2H(alloy) \quad (16)$$

Thus, as the water penetrates through the scale and reaches the metal, it produces the source of oxygen and hydrogen. Therefore, the water charges the Cr-depleted alloy with oxygen and forms FeCr spinel-type oxide in the form of internal oxidation.

A schematic illustration of the breakaway oxidation steps for a pre-oxidised 304L sample exposed to H_2-H_2O at 600 ˚C is shown in Fig. 29. When a sample is pre-oxidised in dry O_2 at 600^{o}C, it forms a $(Fe,Cr,Mn)_3O_4$ overlaying a $(Cr_{1-x}Fe_x)_2O_3$ layer, see Fig. 29a. After oxidising the pre-oxidised sample in the H_2-H_2O environment at 600 ˚C:

- The Cr-rich sub-layer is replaced by almost pure Cr_2O_3, see stage I Fig. 29b.
- The higher oxidation rate of Cr_2O_3 (than $(Cr_{1-x}Fe_x)_2O_3$)) leads to a deeper Cr-depletion zone with critical Cr content/iron activity, see stage II in Fig. 29c.
- Outward diffusion of Fe^{2+} through the formed Cr_2O_3 layer leads to the formation of outward-growing magnetite, see stage III in Fig. 29d.
- The process is followed by the inward diffusion of oxidant species to form an inward-growing layer consisting of a relatively small fraction of fully oxidised FeCr spinel regions and a large fraction of internal FeCr oxides, leaving Fe,Ni metal particles behind (discussed in *Paper V)*, see Fig. 29e.

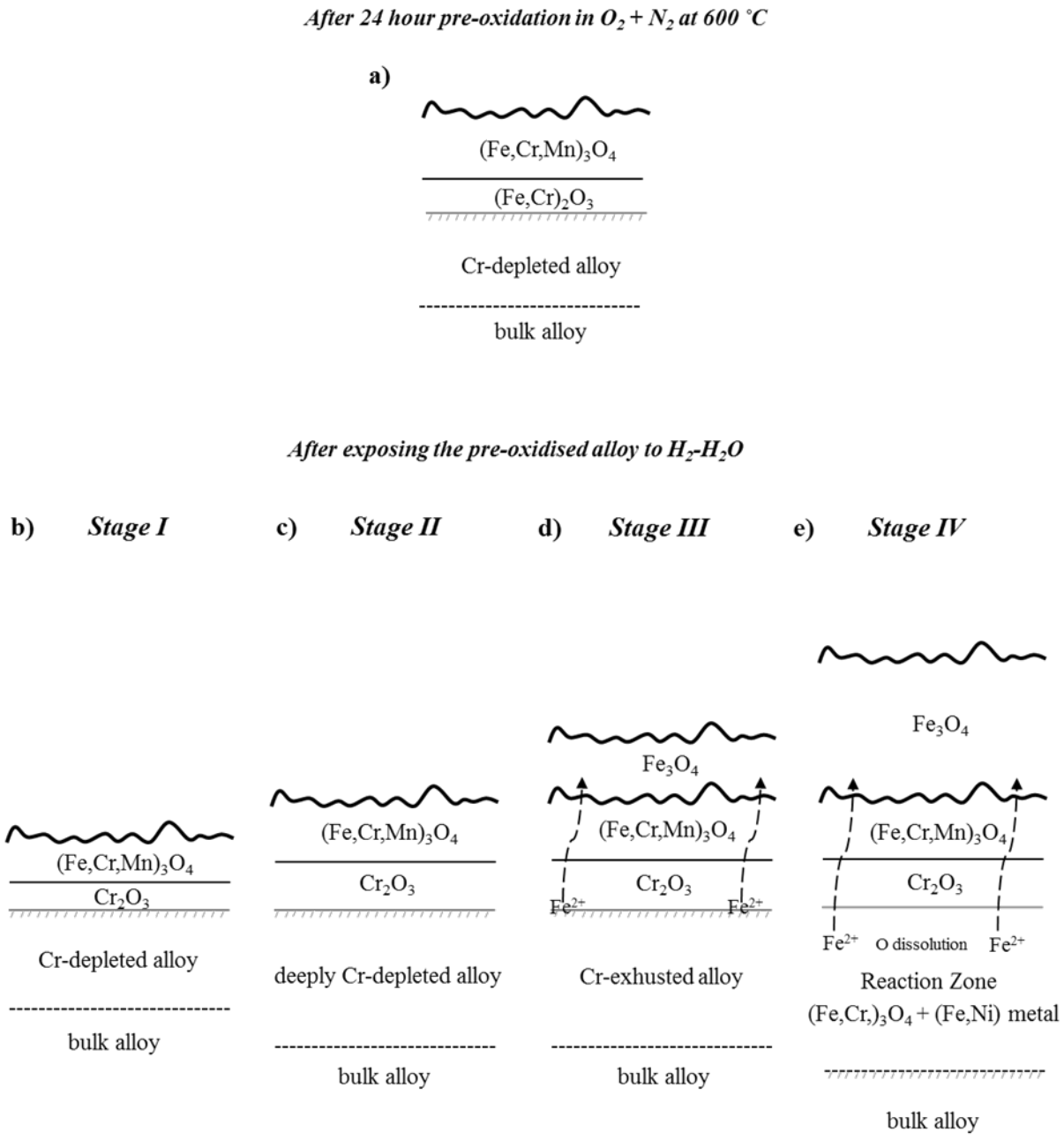

Fig. 29. Schematic illustration of the breakaway oxidation steps for pre-oxidised 304L sample exposed to H_2-H_2O at 600 ˚C.

Earlier studies [70] have shown that the composition of base oxide grains (mainly Fe/Cr ratio) varies substantially from one grain to another. This difference was even found in neighbouring oxide grains where, e.g., in one case, the Cr content was 70 cat.% in one oxide grain and 50 cat.% in the neighbouring oxide grain. Based on thermodynamics, see Fig. 28, the $(Cr_{1-x}Fe_x)_2O_3$ oxide grains containing below approximately 67 cat.% Cr decompose to FeCr spinel-type oxide

and pure Fe after exposure to a low a(O_2) environment, such as 10% H_2- 20% H_2O- Ar . Thus, the different diffusivity of Cr^{3+} and Fe^{2+} in the spinel phase [87, 88] can describe the breakaway oxidation in this case. Since the diffusivity of Cr^{3+} is several orders of magnitude slower than that of Fe^{2+} and O^{2-} in the spinel, those sites may act as open gates for Fe^{2+} and O^{2-}, and the breakaway oxidation results in the formation of an outward-growing magnetite and an inward-growing FeCr spinel oxide.

Breakaway mechanism of non-pre-oxidised samples

The breakaway mechanism of a non-pre-oxidised sample exposed to H_2-H_2O at 600 ˚C is similar to that of the pre-oxidised sample. However, the starting condition is different for these two cases. As shown in *Paper VII,* the initial subscale of the thin oxide that forms in H_2-H_2O at 600 ˚C contains considerably more Cr than the alloy exposed to dry O_2 at the same temperature (see *Paper IV*). TEM results also indicate that the thin scale formed in dry O_2, even after 24 hours (about 30 nm), is thinner than the still protective scale, i.e., thin scale, formed on the alloy in the former environment, i.e., H_2-H_2O, after 1 hour (about 100 nm).

The typical Cr-rich protective oxide which forms in dry O_2 is not thermodynamically stable in the present low a(O_2) environment, see Fig. 28. This is suggested to be the reason why a relatively pure chromia subscale is formed, instead, when exposed to the present reducing environment. As shown, the breakaway oxidation occurred during the first hour of oxidation in H_2-H_2O at 600 ^oC for the non-pre-oxidised sample while the pre-oxidised sample showed protective behaviour within the first hour of oxidation in the same condition. This difference in oxidation behaviour can be described by the reduction process of iron oxide or phase decomposition of $(Cr_{1-x}Fe_x)_2O_3$ (occurring on the pre-oxidised sample), both of which lead to the formation of pure Cr_2O_3 (described in stage I), and are time-consuming processes. Thus, as the $(Cr_{1-x}Fe_x)_2O_3$ is still present on the surface of pre-oxidised samples, it protects the material even in H_2-H_2O at 600 ^oC. However, as it decomposes to Cr_2O_3 (which may take up till 24 hours, see Figure 1 in *Paper IV*), the oxide growth becomes faster. The faster growth of the oxide leads to a deeper Cr depletion zone and is followed by the outward diffusion of divalent iron ions and the inward diffusion of oxidant species.

Thus the breakaway mechanism of non-pre-oxidised 304L exposed to H_2-H_2O at 600 ^oC can be summarised as follows;

- *Stage I*: Relatively pure Cr_2O_3 starts to form on the alloy surface at the initial stage, see Fig. 29b
- *Stage II:* Cr_2O_3 continues to grow, leading to the formation of a Cr-depleted zone at the alloy substrate beneath the oxide, see Fig. 29c.
- *Stage III*: Fe^{2+} ions diffuse outwardly and form Fe_3O_4 on top of the initial thin oxide, see Fig. 29d.
- *Stage IV*: Oxidant species diffuse inwardly and form an inward-growing layer consisting of a relatively small fraction of fully oxidised FeCr spinel regions and a large fraction of internal FeCr oxides, leaving Fe,Ni metal particles behind, see Fig. 29e.

The role of hydrogen The elemental hydrogen generated in the reactions (see Reactions 15 and 16) may form hydride or $H_2(g)$. The generated hydrogen can either be dissolved into the alloy or returned to the gas environment by means of hydrogen evolution occurring at the metal/oxide interface. The role played by hydrogen in the alloy in the oxidation of chromia-forming high-temperature alloys has been discussed by several authors [56, 81, 89]. Most of these authors suggest that dissolved hydrogen has a negative effect on oxidation properties [34, 56, 78, 90]. In the present work, some indications of hydrogen being present beneath the remaining protective oxide were observed (see the dark bands in Figures 9 and 10 in *Paper IV*). Since these indications were not present in the other regions in which the breakaway oxidation had occurred, it is suggested that the dissolved hydrogen may play a role in the transition from slow to rapid oxidation. However, it is cautioned that the dark TEM contrast in Figures 11 and 12 in *Paper IV* does not prove the presence of hydrogen in the alloy. This contrast may also be caused by very small pores or a thinner foil. Further study is planned to address the "hydrogen hypothesis".

9.2.6 Oxide propagation after breakaway (see *Paper V)*

Previous studies [40, 75, 91] have shown that breakaway oxidation of stainless steels in different environments and temperatures results in the formation of a similar scale microstructure consisting of an outward-growing iron oxide and an inner layer with complex oxide and metal features. The inner oxide layer consists of both fully FeCr (Ni) oxide regions, and internal FeCr oxides in addition to the Fe (Ni) metal particles (in between the internal oxide

particles). This type of microstructure has also been reported to be the case for Fe-Cr model alloys from 600 ^{o}C to 900 ^{o}C [27, 37, 55, 81].

This type of scale microstructure was also found in the present study after the breakaway oxidation of 304L in almost all H_2-H_2O environments with different H_2/H_2O ratios. Almost all the scales formed after breakaway oxidation consisted of an outward-growing magnetite, Cr-rich corundum-type oxide at the interface (discussed in Section 9.2.4), and an inward-growing oxide with two distinct oxide microstructures; fully oxidised FeCr spinel oxides and internal FeCr oxide regions (in addition to FeNi metal particles) termed as the ‘’reaction zone’’[74]. The oxide morphology after the breakaway oxidation may be explained by the different diffusivity of Cr^{3+} and Fe^{2+} in the spinel phase [87, 88]. Since the diffusivity of Cr^{3+} is several orders of magnitude slower than that of Fe^{2+} and O^{2-} in the spinel phase, the breakaway oxidation results in the formation of an outward-growing magnetite and an inward-growing FeCr spinel oxide.

Chemical composition of internal oxides As mentioned earlier, the reaction zone consisted of a mixture of internal oxide particles and remaining metal (Fe,Ni) particles. The distribution of these oxide and metal particles can be seen in Fig. 30b. The STEM/EDX line scan through A to B in Fig. 30, in addition to the XRD analysis, revealed that the dark and bright particles are Fe,Cr spinel-type oxide and Fe,Ni metal particles, respectively. The A-B and E-F parts of Fig. 30c, which are in a region close to the steel grain boundary, are also similar to the region depicted in Fig. 30b, i.e., the reaction zone. The overall composition of Fe-Cr internal oxides was about 45 cat.% Cr and 55 cat.% Fe. The phase and chemical composition of the internal oxide is consistent with previous observations of the internal oxidation of Fe-Cr model alloys [37] and commercial alloys [40, 92]. According to the Fe–Cr–O phase diagram, reported in [27], the FeCr spinel oxide exhibits partial solid solubility at 600 °C, a miscibility gap appearing between 9 and 43 cat.% Cr. Thus, the high Cr boundary of the miscibility gap almost coincides with the composition of the internal oxide precipitates in the present findings.

Chemical composition of fully oxidised regions The spinel oxide regions (fully oxidised regions) were found both immediately below the original steel surface and at alloy grain boundaries. An example of the latter region, at the alloy grain boundary, can be seen between

points D and F in Fig. 30c. The region between points B and C are strongly enriched in Fe and Ni with very small amounts of oxygen. The thermodynamic calculations (see *Paper V*) show that Ni is only present in the spinel at an oxygen activity above approximately 10^{-24}. This is in good agreement with the present observations of the formation of fully oxidised regions consisting of FeCr instead of FeCrNi spinel oxides. The latter has been found to form in higher $a(O_2)$ environments, discussed in *Paper V*.

Compared to the alloy composition, the spinel/reaction zones are iron-depleted. This depletion suggested to be the consequence of these regions suppling iron to the formation of outward-growing magnetite.

As discussed in *Paper V*, the general features and microstructure of the scales formed after breakaway are not directly linked to the environment/breakaway mechanism. Instead, they are governed by:

- Different diffusivities of Cr^{3+} and Fe^{2+} in the spinel oxide.
- The appearance of a miscibility gap in the FeCr and FeCrNi spinel oxides
- The equilibrium composition of the spinel (at low $a(O_2)$ Ni is not present in the spinel).

The scale microstructure of 304L samples exposed in the Chalmers gasifier plant (discussed in Section 9.1) after breakaway oxidation was also similar to the laboratory-exposed samples, see Fig. 19. Due to the poor resolution of SEM/EDX analysis, difficulties in obtaining XRD data for the thin oxide (because of the presence of a thick deposit on top), and the small thickness of the oxide layers, it was hard to detect the exact phase and chemical composition of the scale. However, magnetite can be expected to form on top of the scale because of the low $a(O_2)$ of the environment. In addition, the inward-growing layer structure shown in Fig. 19 suggests the presence of reaction zones.

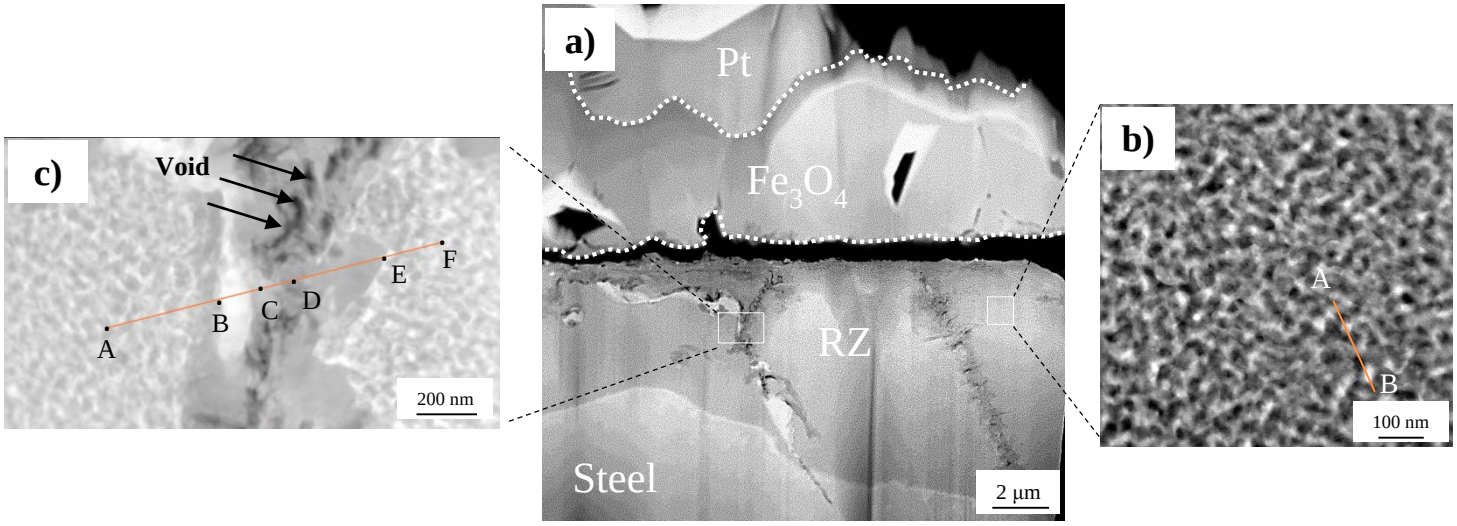

Fig. 30. a) Scanning Transmission Electron Microscope (STEM) High Angle Annular Dark Field (HAADF) image of the cross section of 304L exposed to 10 % H_2-20% H_2O-Ar at 600 °C for 72 hours: b) a zoomed-in micrograph of the marked region in the inner oxide layer, c): A higher magnification of the region close to the grain boundary.

9.2.7 Other alloys *(Paper VI)*

As mentioned in the introduction, the main focus of this study was to investigate the initiation and propagation stages of the oxidation of 304L alloy as a marginal chromia former in H_2-H_2O. This simplified environment was selected as a first step in understanding the corrosion behaviour of (marginal) stainless steels in, e.g., the complex gas mixture of biomass/waste gasifiers.

According to the proposed breakaway mechanism in the present study, an alloy with a considerably higher Cr-level than 304L may show a protective behaviour in H_2-H_2O. Based on the proposed mechanism, one of the key parameters for the occurrence of breakaway oxidation of the alloy in this environment is reaching a critical Cr level/iron activity at the oxide/alloy interface. Thus, if an alloy contains sufficient Cr, and is hindered from reaching critical Cr level/iron activity, the alloy may not suffer from breakaway oxidation. In order to investigate this hypothesis, Sanicro 28, as a high-alloy austenitic stainless steel, was exposed to 10% H_2-20% H_2O- Ar at 600 ˚C (see *Paper VI*). Figure 31 shows a high magnification BSE/SEM cross section image of Sanicro 28 exposed at 600 ºC for 168 hours.

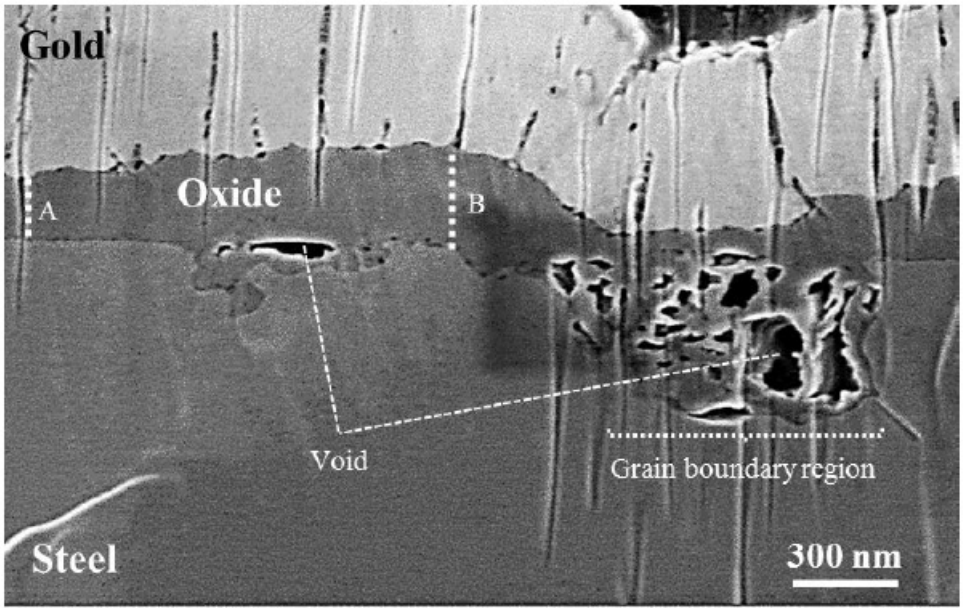

Fig. 31. SEM/BSE cross-sectional view of Sanicro 28 exposed at 600 °C to 10% H_2 - 20% H_2O – Ar for 168 hours. Dashed lines A and B are about 200 and 300 nm, respectively.

As expected, Sanicro 28 performed superior from a corrosion point of view than the 304L grades under the same experimental condition. The oxide scale was very thin even after 168 hours (in comparison with 304L under the same experimental condition). An AES analysis showed the presence of a Cr-rich subscale at the alloy/oxide interface (see *Paper VI*). It is suggested that the subscale of the thin oxide formed on the Sanicro 28 samples is relatively pure chromia (as in the case of 304L). But the reason that breakaway oxidation is not seen on Sanicro 28, under the same experimental condition as 304L, is that Cr-depletion at the alloy substrate beneath the base oxide is not sufficient to cause breakaway oxidation. In other words, the critical Cr level/iron activity has not been reached at the oxide/alloy interface. This is due to a higher reservoir of Cr underneath the oxide, i.e., in the alloy, of Sanicro 28 than 304L. In addition, a comparison between the AES results and the mass gains of Sanicro 28 when exposed to 10% H_2- 20% H_2O- Ar at 600 ˚C (the present results) and those of the alloy when exposed to dry oxygen (shown in [79]) shows that the oxidation rate is higher in the former environment. This is in good agreement with the proposed mechanism in this thesis which suggests a faster growth rate in the reducing environment due to the formation of a relatively pure chromia layer.

The general oxidation behaviour of an alumina former (Kanthal APMT) was also investigated in a 10% H_2- 20% H_2O- Ar environment at 600 ºC. A detailed discussion of this is provided in *Paper VI*. This alloy showed the lowest mass gain of the studied alloys. This is due to the formation of an Al-rich oxide which acts as a highly protective layer in this environment.

A different grade of 304L (18/10) with a higher Ni content was also investigated under the same experimental condition. It was found that the breakaway mechanism of the 304L (18/10) is also in agreement with the proposed mechanism. However, that alloy showed a slower growth rate than the 304L (18/8) alloy. This is suggested to be due to a difference in the chemical composition of the 304L grades, such as in Ni and Si levels.

10 Summary

The corrosion behaviour of 304L stainless steel in H_2/H_2O environments was investigated in detail. The general oxidation behaviour of several alloys in that environment was also studied. The corrosion of 304L stainless steel and a low alloy steel (T22) was studied in the 2MW Chalmers gasifier. Both materials suffered corrosion already after 4h exposure in the gasifier at 600 °C. While parts of the 304L surface was covered by a thin protective oxide scale, the oxide scale had lost its protective properties in other areas and thicker oxide scales had formed. The low-alloy steel (T22) did not form a protective oxide at all and suffered rapid corrosion.

To provide a more detailed understanding of the corrosion mechanism in H_2/H_2O environments, simplified, well-controlled exposures were performed in the laboratory. Prior to the main laboratory exposures an extensive investigation was performed in order to develop experimental procedures that ascertain good control of the experiment and reproducible results. The work investigated the influence of the procedures for start-up and ending the experiments. The findings showed that ppm levels of O_2 can disturb the experiment, causing the formation of unexpected corrosion products. Based on the results obtained from the isothermal oxidation of 304L at 600 °C in H_2-H_2O-Ar environments, it was concluded that:

- Regardless of the H_2/H_2O mixture, 304L stainless steel experienced faster corrosion than reference exposures in 5% O_2.
- At a fixed H_2 concentration, increasing the H_2O concentration led to an increase in oxidation rate.
- When the H_2O content was kept constant, increasing the H_2 concentration resulted in a slight decrease in the oxidation rate, i.e., the environment with the lowest H_2 content, exhibited the highest mass gains.
- Increasing the concentration of the two gases at a fixed H_2O/H_2 ratio increased the oxidation rate.
- Exposure of 304L stainless steel in an H_2O/H_2 environment at 600 °C resulted in the formation of thick, two-layered scales consisting of an outward-growing Fe_3O_4 layer and an inward-growing reaction zone. The latter was made up of a main component consisting of a nm size mixture of FeCr spinel oxide particles and FeNi metal and a minor component consisting of fully oxidised FeCr spinel oxide regions.

The work aimed to explain why H_2O/H_2 environments are much more corrosive than O_2-containing environments towards stainless steels. The findings revealed a new possible mechanism of this effect:

- A relatively pure chromia layer was formed at the initial stage of oxidation in H_2O/H_2.
- The higher growth rate of Cr_2O_3, which forms in H_2-H_2O, than of Cr-rich $(Fe_x,Cr_{1-x})_2O_3$, which forms in, e.g., dry O_2, led to a deeper Cr-depletion of the substrate.
- Eventually the substrate became significantly depleted of Cr, causing the oxidation potential at the scale/substrate interface to increase and allowing Fe to oxidize to Fe^{2+}. The ferrous ions migrated outward, through the grain boundaries in the Cr_2O_3 layer and through the spinel layer, forming outward-growing magnetite on top of the scale.
- Exhaustion of the substrate with respect to Cr also led to the dissolution of oxygen in the alloy and the formation of a partly oxidized reaction zone in the substrate. Most of the reaction zone consisted of a mixture of nm size oxide particles and remaining FeNi metal. In addition, the reaction zone also contained fully oxidised regions.

The Sanicro 28 alloy exhibited protective behaviour in the H_2O/H_2 environment. This was due to its higher chromium reservoir in the bulk of the steel than in that of 304L. In other words, the critical Cr-level needed for breakaway oxidation was not reached in Sanicro 28 at the oxide/alloy interface in the Cr-depleted region.

Of all the alloys investigated, the alumina-forming alloy Kanthal APMT showed the best ability to withstand corrosion in H_2O/H_2 environment. This was attributed to the formation of a thin and protective alumina surface layer.

11 Outlook

The findings in this thesis have provided new knowledge concerning the oxidation mechanism of stainless steels. However, the findings have, in addition, raised new issues to be addressed by future research. A list of future studies are presented below.

- Field exposure in a biomass-fired gasifier:
  - Longer exposures in addition to a more detailed microscopy analysis can improve an understanding of the corrosion behaviour of the studied steels in the system. Also, as mentioned in the discussion section, particle analysis is needed in order to understand the source of the elements which are present in the deposit.

- Laboratory exposure:

  - Some suggestions concerning the role of hydrogen were proposed in *Paper IV*. More analytical techniques applied to the dark regions of the still protective area of a pre-oxidised sample may add more to an understanding about the role of hydrogen in the breakaway oxidation of the studied alloy.

  - A comparison between the thin oxide forms on 304L in H_2- H_2O and dry O_2 at 600 ˚C for 1 hour can strengthen the proposed breakaway mechanism. Therefore, it is suggested to add those results of dry O_2 in the *Paper VII* as a future study.

  - An AES analysis was performed on Sanicro 28 in *Paper VI*. However, due to the low thickness of the oxide and the relatively low resolution of the AES analysis, it is suggested that a TEM analysis of the alloy be performed. A more precise Cr-content of the Cr-rich oxide, in addition to the chemical composition of the Cr-depleted region at the alloy/oxide interface can strengthen the proposed mechanism and explain why breakaway oxidation occurs on 304L but not on Sanicro 28.

  - Transmission Kikuchi Diffraction (TKD) mapping of the subscale of the thin oxide formed in Ar-10 %H_2- 20% H_2O at 600 ˚C is suggested to be done in future research in order to obtain a phase map.

- Synthesis FeCr corundum-type oxides, with different Cr levels, were prepared and oxidised in Ar-10 %H_2- 20% H_2O at 600 ˚C in the present study (not included in the thesis). The results were consistent with the thermodynamic stability of the oxide discussed in Fig. 28. However, the results are pnly indicative, and, therefore it is essential to further investigate this issue with more variation of the Cr level in the oxide.

- In order to obtain a better understanding of the corrosion behaviour of the studied steels in a biomass-fired gasifier, similar studies are needed in CO-CO_2, CO-CO_2-H_2-H_2O and CO-CO_2-H_2-H_2O-H_2S/HCl environments.

12 Acknowledgements

I would like to express my profound gratitude and deep regards to my supervisors Assist. Prof. Jesper Liske and Dr. Torbjörn Jonsson for their exemplary guidance, monitoring and constant encouragement throughout my work.

My sincere gratitude is dedicated to Prof. Lars-Gunnar Johansson and Prof. Jan-Erik Svensson for the support and all the knowledge they have shared with me during these years. This theis would not have been completed without their fruitful collaboration.

Mohammad Sattari is gratefully acknowledged for providing me with valuable TEM analyses. Special thanks to Dr. Josefine Hall for her contribution to the AES measurements. Prof. Vratislav Langer and Prof. Itai Panas are also acknowledged for their fruitful discussions.

Special thanks to Dr. Anders Kvist, Erik Brunius and Esa Väänänen for their technical support and kind regards to Sandra Gustafson and Charlotte Bouveng for their kind assistance with administrative matters.

Moreover, I would like to acknowledge all colleagues and friends at the Environmental Inorganic Chemistry division for their help and support. Their kindness made this journey more enjoyable.

Thanks to Dr. Martin Seeman and colleagues at the Department of Energy and Environment for helping and supporting me with the field exposure at the Chalmers gasifier.

The High Temperature Corrosion Centre (HTC) is acknowledged for providing financial support.

Most importantly, I thank my parents and Mona, for their constant source of love and endless encouragement and support without which this journey would not have been possible.

13 References

1. Higman, C. and M. Burgt, *Gasification*. 2nd ed. 2008, Houston, Texas: Gulf Publishing.
2. Basu, P., *Biomass Gasification and Pyrolysis*. 2010, Elsevier.
3. Pan, T.J. and Y. Niu, *Internal attack of Fe-xCr-10Al alloys induced by the presence of chlorine and sulfur in a reducing atmosphere at 973 K.* Scripta Materialia, 2007. **57**(2): p. 97-100.
4. Krauss, G., *Processing, and Properties of Steels, Properties and Selection: Irons, Steels, and High-Performance Alloys, ASM Handbook*. Vol. 1. 1990: ASM International.
5. Avner, S.H., *Introduction to Physical Metallurgy*. 1964, New York: McGraw-Hill.
6. Calister, W.D.J., *Material Science and Engineering- An Introduction.* 2000(Salt Lake City, UT, USA).
7. Young, D.J., *High temperature oxidation and corrosion of metals*. Corrosion Series, ed. T. Burstein. Vol. 1. 2008, Amsterdam: Elsevier Science.
8. Prescott, R. and M.J. Graham, *The Oxidation of Iron Aluminum-Alloys.* Oxidation of Metals, 1992. **38**(1-2): p. 73-87.
9. Prescott, R. and M.J. Graham, *The Formation of Aluminum-Oxide Scales on High-Temperature Alloys.* Oxidation of Metals, 1992. **38**(3-4): p. 233-254.
10. Kofstad, P., *High Temperature Corrosion*. 1998, London: Elsevier Applied Science.
11. Khanna, A.S., *introduction to High Temperature Oxidation and Corrosion*. Materials Park, OH, US: ASM International.
12. *http://oregonstate.edu/instruct/me581/Homework/Overheads/Ellingham.jpg*.
13. Wagner, C., *The theory of the warm-up process.* Zeitschrift Fur Physikalische Chemie-Abteilung B-Chemie Der Elementarprozesse Aufbau Der Materie, 1933. **21**(1/2): p. 25-41.
14. Wagner, C., *The theory of the warm-up process.*
15. Birks, N., G.H. Meier, and F.S. Pettit, *Introduction to high temperature oxidation of metals.* 2006.
16. Asteman, H., E. Ahlberg, and S. J-E, *Electric properties of Fe2O3, Cr2O3, and (Cr,Fe)2O3 and their relevance to corrosion.* Electrochemical Society.
17. Klumpes, R., C.H.M. Maree, E. Schramm, and J.H.W. deWit, *The influence of chromium on the oxidation of beta-NiAl at 1000 degrees C.* Werkstoffe Und Korrosion-Materials and Corrosion, 1996. **47**(11): p. 619-624.
18. Brumm, M.W. and H.J. Grabke, *The Oxidation Behavior of Nial .1. Phase-Transformations in the Alumina Scale during Oxidation of Nial and Nial-Cr Alloys.* Corrosion Science, 1992. **33**(11): p. 1677-&.
19. Stott, F.H., G.C. Wood, and J. Stringer, *The Influence of Alloying Elements on the Development and Maintenance of Protective Scales.* Oxidation of Metals, 1995. **44**(1-2): p. 113-145.
20. Berthome, G., E. N'Dah, Y. Wouters, and A. Galerie, *Temperature dependence of metastable alumina formation during thermal oxidation of FeCrAl foils.* Materials and Corrosion-Werkstoffe Und Korrosion, 2005. **56**(6): p. 389-392.
21. Josefsson, H., F. Liu, J.E. Svensson, M. Halvarsson, and L.G. Johansson, *Oxidation of FeCrAl alloys at 500-900 degrees C in dry O-2.* Materials and Corrosion-Werkstoffe Und Korrosion, 2005. **56**(11): p. 801-805.
22. Liu, F., H. Josefsson, J.E. Svensson, L.G. Johansson, and M. Halvarsson, *TEM investigation of the oxide scales formed on a FeCrAlRE alloy (Kanthal AF) at 900 degrees C in dry O-2 and O-2 with 40% H2O.* Materials at High Temperatures, 2005. **22**(3-4): p. 521-526.
23. Quadakkers, W.J., J.F. Norton, S. Canetoli, K. schuster, and A. Gil, in *3rd International Conference on Microscopy of Oxidation*. 1996: The Institute of Materials: Cambridge. p. 609-619.
24. Hansel, M., W.J. Quadakkers, and D.J. Young, *Role of water vapor in chromia-scale growth at low oxygen partial pressure.* Oxidation of Metals, 2003. **59**(3-4): p. 285-301.
25. Henry, S., J. Mougin, Y. Wouters, J.P. Petit, and A. Galerie, *Characterization of chromia scales grown on pure chromium in different oxidizing atmospheres.* Materials at High Temperatures, 2000. **17**(2): p. 231-234.

26. Hultquist, G., B. Tveten, and E. Hornlund, *Hydrogen in chromium: Influence on the high-temperature oxidation kinetics in H2O, oxide-growth mechanisms, and scale adherence.* Oxidation of Metals, 2000. **54**(1-2): p. 1-10.
27. Pujilaksono, B., T. Jonsson, H. Heidari, M. Halvarsson, J.E. Svensson, and L.G. Johansson, *Oxidation of Binary FeCr Alloys (Fe-2.25Cr, Fe-10Cr, Fe-18Cr and Fe-25Cr) in O-2 and in O-2 + H2O Environment at 600 degrees C.* Oxidation of Metals, 2011. **75**(3-4): p. 183-207.
28. Tveten, B., G. Hultquist, and T. Norby, *Hydrogen in chromium: Influence on the high-temperature oxidation kinetics in O-2, oxide-growth mechanisms, and scale adherence.* Oxidation of Metals, 1999. **51**(3-4): p. 221-233.
29. Young, D.J. and H.Y. Yin, *Water Vapour Effects on FeO Scale Growth: Differences Between Iron and Steel.* Oxidation of Metals, 2013. **79**(5-6): p. 445-460.
30. A. Rahmel and J. Tobolski, *Einfluss von Wasserdampf und Kohlendioxyd auf die Oxydation von Eisen in Saurstoff bei Hohen Temperaturen.* Corrosion science, 1965. **5**: p. 333-346.
31. Pujilaksono, B., T. Jonsson, M. Halvarsson, J.E. Svensson, and L.G. Johansson, *Oxidation of iron at 400-600 degrees C in dry and wet O-2.* Corrosion Science, 2010. **52**(5): p. 1560-1569.
32. Wallinder, D., E. Hornlund, and G. Hultquist, *Influence of hydrogen in iron and in two stainless steels on aqueous and gaseous corrosion.* Journal of the Electrochemical Society, 2002. **149**(9): p. B393-B397.
33. Yin, H., W.Y.D. Yuen, and D.J. Young, *Effects of water vapour and oxygen partial pressures on low carbon steel oxidation in N2-H2-H2O mixtures.* Materials and Corrosion-Werkstoffe Und Korrosion, 2012. **63**(10): p. 869-877.
34. J. Ehlers, D. J. Young, E. J. Smaardijk, A. K. Tyagi, H. J. Penkalla, L. Singheiser, and W.J. Quadakkers, *Enhanced oxidation of the 9%Cr Steel P91 in water vapor containing environment.* Corrosion science, 2006. **48**: p. 3428-3454.
35. Othman, N.K., N. Othman, J. Zhang, and D.J. Young, *Effects of water vapour on isothermal oxidation of chromia-forming alloys in Ar/O-2 and Ar/H-2 atmospheres.* Corrosion Science, 2009. **51**(12): p. 3039-3049.
36. M. Schutze, M. Schorr, D. P. Renusch, A. Donchev, and J.P.T. Vossen, Materials Research, 2004. **7**(1): p. 111-123.
37. Jonsson, T., B. Pujilaksono, H. Heidari, F. Liu, J.E. Svensson, M. Halvarsson, and L.G. Johansson, *Oxidation of Fe-10Cr in O-2 and in O-2+H2O environment at 600 degrees C: A microstructural investigation.* Corrosion Science, 2013. **75**: p. 326-336.
38. Yin, H., S.L.I. Chan, W.Y.D. Yuen, and D.J. Young, *Temperature Effects on the Oxidation of Low Carbon Steel in N-2-H-2-H2O at 800-1200 degrees C.* Oxidation of Metals, 2012. **77**(5-6): p. 305-323.
39. H. Asteman, S. J-E, M. Norell, and J. L-G, *Influence of water vapor and flow rate on the High Temperature Oxidation of 304L; Effect of Chromium oxide hydroxide evaporation.* Oxidition of Metals, 2000. **54**.
40. Hansson, A.N., K. Pantleon, F.B. Grumsen, and M.A.J. Somers, *Microstructure Evolution During Steam Oxidation of a Nb Stabilized Austenitic Stainless Steel.* Oxidation of Metals, 2010. **73**(1-2): p. 289-309.
41. Henry, S., A. Galerie, and L. Antoni, *Abnormal oxidation of stabilized ferritic stainless steels in water vapor.* High Temperature Corrosion and Protection of Materials 5, Pts 1 and 2, 2001. **369-3**: p. 353-360.
42. Fujii, C.T. and R.A. Meussner, *The Mechanism of the High-Temperature Oxidation of Iron-Chromium Alloys in Water Vapor.* Journal of the Electrochemical Society, 1964. **111**(11): p. 1215-1221.
43. Fujii, C.T. and R.A. Meussner, *Oxide Structures Produced on Iron-Chromium Alloys by a Dissociative Mechanism.* Journal of the Electrochemical Society, 1963. **110**(12): p. 1195-1204.
44. Essuman, E., *Dissertation*. 2008, University of Oslo, Norway.
45. Nickel, H., Y. Wouters, M. Thiele, and W.J. Quadakkers, *The effect of water vapor on the oxidation behavior of 9%Cr steels in simulated combustion gases.* Fresenius Journal of Analytical Chemistry, 1998. **361**(6-7): p. 540-544.
46. Evans, H.E., A.T. Donaldson, and T.C. Gilmour, *Mechanisms of breakaway oxidation and application to a chromia-forming steel.* Oxidation of Metals, 1999. **52**(5-6): p. 379-402.

47. Asteman, H., J.E. Svensson, L.G. Johansson, and M. Norell, *Indication of chromium oxide hydroxide evaporation during oxidation of 304L at 873 K in the presence of 10% water vapor*. Oxidation of Metals, 1999. **52**(1-2): p. 95-111.
48. Asteman, H., J.E. Svensson, and L.G. Johansson, *Evidence for chromium evaporation influencing the oxidation of 304L: The effect of temperature and flow rate*. Oxidation of Metals, 2002. **57**(3-4): p. 193-216.
49. Tveten, B., G. Hultquist, and D. Wallinder, *Hydrogen and yttria in chromium: Influence on the high-temperature oxidation kinetics in O-2, oxide-growth mechanisms and scale adherence.* Oxidation of Metals, 2001. **55**(3-4): p. 279-289.
50. K. Nakagawa, Y. Matsunaga, and T. Yanagisawa, *Corrosion behavior of ferritic steels on the air sides of boiler tubes in a steam/air dual environment.* Materials at High Temperature, 2003. **20**: p. 67-73.
51. Nakai, M., K. Nagai, Y. Murata, M. Morinaga, S. Matsuda, and M. Kanno, *Correlation of high-temperature steam oxidation with hydrogen dissolution in pure iron and ternary high-chromium ferritic steel.* Isij International, 2005. **45**(7): p. 1066-1072.
52. Schutze, M., D. Renusch, and M. Schorr, *Parameters determining the breakaway oxidation behaviour of ferritic martensitic 9%Cr steels in environments containing H2O.* Corrosion Engineering Science and Technology, 2004. **39**(2): p. 157-166.
53. Schütze, M., M. Schorr, D.P. Renusch, A. Donchev, and J.P.T. Vossen, *The role of alloy composition, environment and stresses for the oxidation resistance of modern 9% Cr steels for fossil power stations.* Materials Research, 2004. **7**(1): p. 111-123.
54. Thiele, M., H. Teichmann, W. Schwarz, and W.J. Quadakkers, VGB Kraftwerkstechnik, 1997. **77**: p. 135.
55. Essuman, E., G.H. Meier, J. Zurek, M. Hansel, L. Singheiser, and W.J. Quadakkers, *Enhanced internal oxidation as trigger for breakaway oxidation of Fe-Cr alloys in gases containing water vapor*. Scripta Materialia, 2007. **57**(9): p. 845-848.
56. Essuman, E., G.H. Meier, J. Zurek, M. Hansel, and W.J. Quadakkers, *The effect of water vapor on selective oxidation of Fe-Cr alloys.* Oxidation of Metals, 2008. **69**(3-4): p. 143-162.
57. Israelsson, N., J. Engkvist, K. Hellstrom, M. Halvarsson, J.E. Svensson, and L.G. Johansson, *KCl-Induced Corrosion of an FeCrAl Alloy at 600 A degrees C in O-2 + H2O Environment: The Effect of Pre-oxidation.* Oxidation of Metals, 2015. **83**(1-2): p. 29-53.
58. Canovic, S., J. Engkvist, F. Liu, H. Lai, H. Gotlind, K. Hellstrom, J.E. Svensson, L.G. Johansson, M. Olsson, and M. Halvarsson, *Microstructural Investigation of the Initial Oxidation of the FeCrAlRE Alloy Kanthal AF in Dry and Wet O-2 at 600 and 800 degrees C.* Journal of the Electrochemical Society, 2010. **157**(6): p. C223-C230.
59. Gotlind, H., F. Liu, J.E. Svensson, M. Halvarsson, and L.G. Johansson, *The effect of water vapor on the initial stages of oxidation of the FeCrAl alloy Kanthal AF at 900 degrees C.* Oxidation of Metals, 2007. **67**(5-6): p. 251-266.
60. Kallstrom, R., *Corrosion during Gasification of Biomass and Waste.* Journal De Physique Iv, 1993. **3**(C9): p. 751-761.
61. Lai, G., *High Temperature Corrosion and Material Applications*. 2007: ASM International.
62. Elger, R. and L. J, *High Temperature Corrosion in Gasification Environment Using Biomass and Waste as fuel*. literature study, 2011.
63. Bakker, W.T., *Materials Research.* 2004.
64. Goldstein, J., D. Newbury, D. Joy, and e. all, *Scaning Electron Microscopy and X-Ray Microanalysis.* 2007(Third edition).
65. West, A.R., *Basic Solid State Chemistry*. **Second Edition**.
66. Jonsson, T., *Microscopy of High Temperature Oxidation of Iron and Some Stainless Steels.*
67. Bagshaw, H., *Scanning Electron Microscopy.* Center for Microscopy and Analysis (CMA).
68. *http://www.cambridge-sensotec.co.uk/gallery/InstructionManualPDF/Rapidox_2100ZR_Instruction_Manual_version_3.5.pdf*.
69. Pettersson, J., H. Asteman, J.E. Svensson, and L.G. Johansson, *KCl induced corrosion of a 304-type austenitic stainless steel at 600 degrees C; The role of potassium.* Oxidation of Metals, 2005. **64**(1-2): p. 23-41.

70. Tang, J.E., M. Halvarsson, H. Asteman, and J.E. Svensson, *The microstructure of the base oxide on 304L steel.* Micron, 2001. **32**(8): p. 799-805.
71. Sahri, M.I., N.K. Othman, Z. Samsu, and A.R. Daud, *Investigation of High Temperature Corrosion Behavior on 304L Austenite Stainless Steel in Corrosive Environments.* 2014 Ukm Fst Postgraduate Colloquium: Proceedings of the Universiti Kebangsaan Malaysia, Faculty of Science and Technology 2014 Postgraduate Colloquium, 2014. **1614**: p. 152-157.
72. Lussana, D., D. Baldissin, M. Massazza, and M. Baricco, *Thermodynamic and Kinetics Aspects of High Temperature Oxidation on a 304L Stainless Steel.* Oxidation of Metals, 2014. **81**(5-6): p. 515-528.
73. T. Jonsson and e. al, *The influence of KCl on the corrosion of an austenitic stainless steel (304L) in oxidizing humid conditions at 600C: A Microstructural study.* Oxidation of Metals, 2009. **72**: p. 213-239.
74. Jonsson, T., S. Karlsson, H. Hooshyar, M. Sattari, J. Liske, J.E. Svensson, and L.G. Johanson, *Oxidation after breakdown of the chromium rich scale on stainless steels at high temperature – internal oxidation.* Submitted to Oxidation of Metals, 2015.
75. M. Halvarsson, J. E. Tang, H. Asteman, J. E. Svensson, and L-G. Johansson, *Microstructural investigation of the breakdown of the protective oxide scale on a 304L steel in the presence of oxygen and water vapor at 600C.* Corrosion science, 2006. **48**: p. 2014-2035.
76. J. Topfer, S. Aggarwal, and R. Dieckmann, *Point defects and cation tracer diffusion in (CRXFE1-X)(3-Delta)O-4 spinels.* Solid State Ionics, 1995. **81**: p. 251-266.
77. N. Folkeson, T. Jonsson, M. Halvarsson, L.-G. Johansson, and S. J-E, *The influence of small amounts of KCl on the high temperature corrosion of Fe-2.25Cr-1Mo steel at 400 and 500 degree C.* Materials and Corrosion-Werkstoffe und Korrosion, 2011. **62**: p. 606-615.
78. Quadakkers, W.J. and J. Zurek, *Oxidation in Steam and Steam/Hydrogen Environment.* 2010.
79. Pettersson, C., T. Jonsson, C. Proff, M. Halvarsson, J.E. Svensson, and L.G. Johansson, *High Temperature Oxidation of the Austenitic (35Fe27Cr31Ni) Alloy Sanicro 28 in O-2 + H2O Environment.* Oxidation of Metals, 2010. **74**(1-2): p. 93-111.
80. Opila, E.J., N.S. Jacobson, D.L. Myers, and E.H. Copland, *Predicting oxide stability in high-temperature water vapor.* Jom, 2006. **58**(1): p. 22-28.
81. Othman, N.K., J.Q. Zhang, and D.J. Young, *Water Vapour Effects on Fe-Cr Alloy Oxidation.* Oxidation of Metals, 2010. **73**(1-2): p. 337-352.
82. Andersson, J.O., T. Helander, L.H. Hoglund, P.F. Shi, and B. Sundman, *THERMO-CALC & DICTRA, computational tools for materials science.* Calphad-Computer Coupling of Phase Diagrams and Thermochemistry, 2002. **26**(2): p. 273-312.
83. Pujilaksono, B., T. Jonsson, M. Halvarsson, I. Panas, J.E. Svensson, and L.G. Johansson, *Paralinear oxidation of chromium in O(2)+H(2)O environment at 600-700 degrees C.* Oxidation of Metals, 2008. **70**(3-4): p. 163-188.
84. Tang, J.E., F. Liu, H. Asteman, J.E. Svensson, L.G. Johansson, and M. Halvarsson, *Investigation of FIB-thinned TEM cross-sections of oxide scales formed on type 310 steel at 600 degrees C in water vapour-containing oxygen atmospheres.* Materials at High Temperatures, 2007. **24**(1): p. 27-55.
85. Canovic, S., J. Froitzheim, R. Sachitanand, M. Nikumaa, M. Halvarsson, L.G. Johansson, and J.E. Svensson, *Oxidation of Co- and Ce-nanocoated FeCr steels: A microstructural investigation.* Surface & Coatings Technology, 2013. **215**: p. 62-74.
86. Lindgren, M. and I. Panas, *On the fate of hydrogen during zirconium oxidation by water: effect of oxygen dissolution in alpha-Zr.* Rsc Advances, 2014. **4**(22): p. 11050-11058.
87. Topfer, J., S. Aggarwal, and R. Dieckmann, *Point-Defects and Cation Tracer Diffusion in (Crxfe1-X)(3-Delta)O-4 Spinels.* Solid State Ionics, 1995. **81**(3-4): p. 251-266.
88. Van Orman, J.A. and K.L. Crispin, *Diffusion in Oxides.* Diffusion in Minerals and Melts, 2010. **72**: p. 757-825.
89. Akermark, T. and G. Hultquist, *Oxygen exchange in oxidation of an Fe-20Cr-10Al alloy in similar to 10 mbar O-2/H2O-gas mixtures at 920 degrees C.* Oxidation of Metals, 1997. **47**(1-2): p. 117-137.
90. Quadakkers, W.J., J. Zurek, and M. Hänsel, *Effect of water vapor on high temperature oxidation of FeCr alloys.* JOM, 2009. **61**: p. 44-50.

91. Young, D.J., J. Zurek, L. Singheiser, and W.J. Quadakkers, *Temperature dependence of oxide scale formation on high-Cr ferritic steels in Ar-H-2-H2O.* Corrosion Science, 2011. **53**(6): p. 2131-2141.
92. Halvarsson, M., J.E. Tang, H. Asteman, J.E. Svensson, and L.G. Johansson, *Microstructural investigation of the breakdown of the protective oxide scale on a 304 steel in the presence of oxygen and water vapour at 600 degrees C.* Corrosion Science, 2006. **48**(8): p. 2014-2035.